Transverse and Longitudinal Degradations in Ceramic Solid Electrolytes

Published as part of the Virtual Special Issue "John Goodenough at 100".

Yanhao Dong,* I-Wei Chen,* and Ju Li*

Read Online

ACCESS | Metrics & More | Article Recommendations

ABSTRACT: Ceramic solid electrolytes conducting primarily a specific ion but with minuscule electron leakage are used in many electrochemical devices. Their degradation phenomena may be classified into two broad categories—a slow transverse mode accumulating damage normal to the ionic current direction and a fast longitudinal mode accumulating degradation parallel to the current direction. Examples of the transverse mode include oxygen bubbles on transverse grain boundaries, in-plane electrolyte cracking in solid oxide electrolysis cells, and cathodic reduction of beta-alumina electrolytes in Na−S batteries. Examples of the longitudinal mode include short-circuiting dendrite formation in metal batteries of both the Na−S type and the all-solid-state lithium metal type. Analogous instability modes are also seen in field-assisted ceramic processing, dielectric devices, and memristors. These phenomenological similarities across different devices, operating conditions, and technologies, as well as the origins of their damage mechanisms, can be understood in terms of the highly nonlinear spatial distributions of the minority carriers (electron/hole) and the chemical potential of the equivalent charge-neutral species such as O_2; such distributions can in turn cause or exacerbate damaging concentrations of stress and electric fields. This review also outlines strategies for improving material designs to mitigate degradation, which will be especially important for operations and applications under extreme electrochemical conditions.
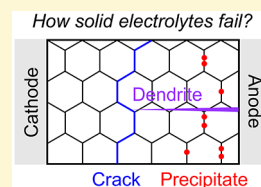
1. INTRODUCTION

Ceramic solid electrolytes as fast ion conductors have found many electrochemical applications in solid oxide fuel cells/electrolysis cells (SOFCs/SOECs), oxygen sensors, protonic ceramic fuel cells/electrolysis cells (PCFCs/PCECs), all-solid-state batteries, and solid-state ion pumps.[1−5] To serve these applications, they must be good ionic conductors and poor electronic conductors under normal operation conditions, i.e., having an ionic transference number very close to one. However, electronic leakage may arise at more extreme redox conditions, which defines the electrolytic window for normal operation, and operation outside the window will result in a lowered open-circuit voltage (OCV) as well as lowered Faraday efficiency and energy efficiency. Electrolyte degradation may ensue in such operations, but it may also occur over an extended service life in relatively normal operations. Moreover, more rapid degradation happens under excessive/extreme conditions, for example, high current densities of the SOEC and PCEC and high-rate charging of alkali metal batteries. Historically, one of the first well-known examples of electrolyte degradation is dendrite formation in beta-alumina solid electrolytes in Na−S batteries, and the same phenomena have been seen in oxide, sulfide, and halide electrolytes in all-solid-state lithium metal batteries recently.[6−9] Another well-known example is cracking in yttria-stabilized zirconia (YSZ) electrolytes in SOEC after many duty cycles.[2,10−13] Clearly, understanding the phenomenology and

origin of electrolyte degradation is important for electrochemical applications of ceramic solid electrolytes.

Microstructurally, it is convenient to distinguish two types of degradation phenomena in ceramic solid electrolytes, a longitudinal mode that accumulates damage along the current direction and a transverse mode that accumulates damage perpendicular to the current direction. Within each mode, the damage phenomena found in different devices under vastly different operating conditions are surprisingly similar to each other. For example, degradations with a similar appearance are seen in SOFCs/SOECs at 800−1000 °C, Na−S batteries at ∼300 °C, and all-solid-state batteries at ambient temperatures. It turns out the phenomenological analogy also extends to structural evolutions found in field-assisted ceramic processing above 1000 °C, ambient dielectrics under a high voltage, and nanofilm ceramic memristors manifesting resistance switching enabled by either ion diffusion or mixed ion/electron conduction. Understanding such commonality will help

design/engineer new damage-mitigating strategies and materials/devices.

Fundamentally, degradation is triggered by some instability in solid electrolytes when the latter's condition is far from ideal in the following ways. First, the redox potential inside the electrolyte may severely deviate from a linear interpolation between the two electrode potentials; indeed, it may assume a shock-like distribution along the electrolyte-thickness direction. The redox potential here is the electronic electrochemical potential or Fermi energy E_F, which consists of not only a nearly linear electrostatic contribution but also a highly nonlinear term that is strongly dependent on the electron/hole concentrations. These concentrations reach local thermodynamic equilibrium with ionic disorders (vacancies and interstitials) commonly illustrated using the Brouwer diagram. The nonlinearity originates in the Brouwer diagram that correlates the ionic disordering with PO_2, the oxygen partial pressure, and it features an extremely sharp "V-shaped" minimum of the electron–hole concentration/conductivity at an intermediate PO_2—or its Na/Li equivalent. Second, the stress inside the electrolyte may not be zero; instead it may be nonuniformly distributed, sometimes with an acute concentration at certain defects or discontinuities. Third, the electric field and current inside the electrolyte may not be uniform either when the cell is not at a steady-state or, again, when there are flaws.

As will become clear later, synergism between the above three may complicate and exacerbate the nonideal conditions. As a simplification, the field and current in the solid electrolyte can be considered to be one-dimensional, which sets the direction of the current along the coordinate x. This is because the electrolyte is usually a thin membrane operating mostly in the ohmic regime with a resistance proportional to the thickness L and inversely proportional to the area A. Thus, as long as the membrane is processable and mechanically strong enough, its L/A ratio is kept small to minimize the internal loss and the voltage load. In such a geometry, transverse degradation is the same as in-plane damage; for example, in-plane cracking of the membrane is a transverse degradation. In contrast, a cross-electrode dendrite is a longitudinal degradation. Below we will show that the majority of known degradation types in various applications belong to one of these two modes, while most of the remaining types may be thought of as either a mixed-mode degradation due to mode–mode coupling or a damage-mode-induced interface instability. We will also show that a typical origin of these degradation modes resides in the departure of the redox potential and stress/field/current distributions from the ideal condition.

2. SOFC/SOEC

2.1. Overview of Damage Mechanisms. SOFC converts the chemical energy of oxidizing a fuel, often in the gas form, to electricity. Being separated by a dense ion-conducting and nearly electron-insulating ceramic electrolyte, the two porous electrodes conduct the two half-cell reactions separately—oxidation in the fuel electrode and reduction in the air electrode—thus forcing the electronic current to flow in the external circuit. SOFC can also be reversely operated by applying an external voltage exceeding the OCV. This enables electrolysis, and such a cell is known as an SOEC, which uses electricity to produce chemicals. For O^{2-}-based SOFCs/SOECs that operate above 800 °C, YSZ is the preferred electrolyte material because of its high O^{2-} conductivity and low electronic conductivity—for both electron and hole—over a very large electrochemical

stability window. In contrast, ceria-based electrolytes (e.g., Gd-doped CeO_2, GDC) have a smaller electrolytic window, limited by electron conductivity that arises from Ce^{4+} to Ce^{3+} reduction, but it can still be used at 600–800 °C to utilize its higher O^{2-} conductivity. Meanwhile, because of a better chemical compatibility than YSZ's, the GDC electrolyte, or a GDC buffer layer alone (between YSZ and cathodes), allows more active and thus more efficient cathodes (e.g., $La_{0.6}Sr_{0.4}Co_{0.2}Fe_{0.8}O_{3-\delta}$, LSCF, and $Ba_{0.5}Sr_{0.5}Co_{0.8}Fe_{0.2}O_{3-\delta}$, BSCF) to be used. As a result, the electrode overpotentials are lowered, which helps mitigate internal damage in general. Another promising electrolyte is doped $LaGaO_3$ (e.g., $La_{0.9}Sr_{0.1}Ga_{0.8}Mg_{0.2}O_{3-\delta}$, LSGM), which is under development for intermediate-temperature applications.[14−16] Its negligible electronic conductivity and high ionic conductivity in a broad range of temperatures and oxygen partial pressures[17] make LSGM more stable than GDC, especially on the reducing side.

Since the half-cell reactions in SOFC and SOEC proceed in opposite directions, their electrode overpotentials have opposite signs. For example, if H_2 is fed on the fuel electrode side and air on the oxygen electrode side, then the magnitude of oxygen potential μ_{O_2} (i.e., the chemical potential of oxygen molecule O_2, which is related to the equilibrium PO_2) at the oxygen electrode−electrolyte interface under different operation modes ranks in the order of $\mu_{O_2}^{SOEC} > \mu_{O_2}^{OCV} > \mu_{O_2}^{SOFC}$, and the oxygen potential at the fuel electrode−electrolyte interface follows $\mu_{O_2}^{SOEC} < \mu_{O_2}^{OCV} < \mu_{O_2}^{SOFC}$. Physically, this means that, compared to SOFC, SOEC's oxygen electrode side is more oxidizing and its fuel electrode side more reducing, and moreso the larger the imposed SOEC current density. Inasmuch as these oxygen potentials set the boundary conditions of the electrolyte and more extreme boundary conditions will likely lead to more degradations, one should expect more degradation in high-current-density SOECs.

Within the electrolyte, O^{2-} moves from the oxygen electrode to the fuel electrode in SOFC, and in SOEC the direction of O^{2-} flow as well as that of the electrical field is reversed. Despite the fact that the electrolyte is a fast ion conductor, in reality, in both SOFC and SOEC there is always a minor electronic current (thus a small electronic leakage current) flowing from the oxygen electrode to the fuel electrode through the solid electrolyte. The direction is set by the electron's electrochemical potential, which is always higher on the fuel electrode side than on the air electrode side.[18] (The electronic current is delivered by either positively charged hole polarons in the same direction of the current or negatively charged electron polarons in the opposite direction of the current.) At an ideal steady state where there can be no Faradaic reaction internally, the ionic and electronic currents must be locally divergence-free, $\nabla \cdot \boldsymbol{J}_i = 0$ and $\nabla \cdot \boldsymbol{J}_e = 0$. With the one-dimensional approximation, we therefore must have $\boldsymbol{J}_i = J_i \mathbf{e}_x$ and $\boldsymbol{J}_e = J_e \mathbf{e}_x$, where $\mathbf{e}_x$ is the unit vector and both J_i and J_e are x-independent constants. While J_e could be very small in magnitude compared to J_i, it is nonzero because the electronic conductivity, while very small compared to the ionic conductivity and spatially highly nonuniform, is never zero anywhere according to the Brouwer diagram. Indeed, $J_i(x) = \text{const}_1$ and $J_e(x) = \text{const}_2$ must be present to maintain local equilibrium inside the electrolyte. Because $J_e(x) = \sigma_e(x)(\partial E_F/\partial x)/e$, where the electronic conductivity $\sigma_e(x) > 0$ is highly nonuniform in x according to the Brouwer diagram (since $\sigma_e(x) = \sigma_e(PO_2(x))$ with a typical power-law dependence and $PO_2(x)$ itself changes inside the electrolyte along with $E_F(x)$), the
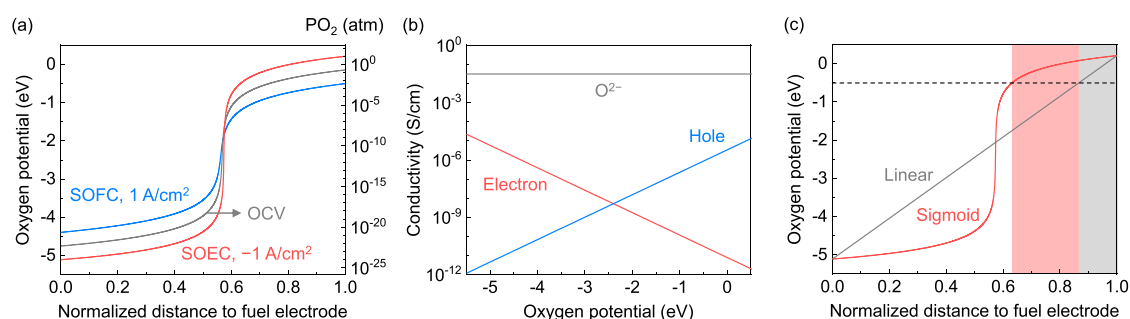
Figure 1. (a) Calculated oxygen potential distribution inside a 10 μm-thick YSZ electrolyte under OCV, SOFC (at 1 A/cm^2), and SOEC (at −1 A/cm^2) modes at 800 °C. Boundary oxygen potentials were set as −4.7531 eV at the fuel electrode/electrolyte interface and −0.1443 eV at the oxygen electrode/electrolyte interface under OCV, −4.3959 eV at the fuel electrode/electrolyte interface and −0.5015 eV at the oxygen electrode/electrolyte interface under SOFC, and −5.1103 eV at the fuel electrode/electrolyte interface and 0.2129 eV at the oxygen electrode/electrolyte interface under SOEC. Oxygen potential set as 0 eV at 1 atm oxygen partial pressure. (b) Conductivity of O^{2-}, electron, and hole of YSZ at a function of oxygen potential at 800 °C taken from ref 21. (c) Comparison of a sigmoidal vs a linear oxygen potential profile. Shaded regions denote the regions with oxygen potential above −0.5 eV.

implication of the solution const$_2$ = $\sigma_e(x)(\partial E_F/\partial x)/e$ is that $\partial E_F/\partial x$ *must be highly nonuniform as well*, reaching a maximum near the "V-shaped" population minimum of the electronic disorder in the Brouwer diagram. Thus, it is the ionic and electronic conductivities together that dictate the steady-state spatial distribution of the oxygen potential $\mu_{O_2}(x) = \mu_{O_2}^\Theta + k_B T \ln PO_2(x)$ and $E_F(x)$ profiles.

It turns out that as the electrode-overpotential/current increases, the oxygen potential increasingly takes a more nonlinear sigmoidal shape as shown in Figure 1a.[19,20] To understand the origin of the nonlinearity, we recall that a good, fast-ion conducting electrolyte such as YSZ at the operation temperature of SOFC/SOEC has a set of very high and constant O^{2-} concentrations and O^{2-} conductivities, so its electric field is very small. Therefore, to drive even a tiny but nevertheless spatially uniform nonzero electronic current everywhere, the driving force must mainly come from the concentration-gradient term of the electronic disorder that affects $\partial E_F/\partial x$ (i.e., concentration polarization, recalling that electronic-disorder and ionic-disorder concentrations are correlated). As shown in Figure 1a, somewhere in the middle of the electrolyte, this gradient becomes especially large, and the potential takes the shape of a concentration shock. This is because the V-shaped electronic conductivity minimum (far lower than the corresponding ionic conductivity) in the Brouwer diagram,[21] depicted in Figure 1b, occurs right there, thus necessitating a maximal driving force at that location. Indeed, as shown in Figure 1a, the potential is almost shaped like a step function. It is this step-like potential that allows (a) the high-PO$_2$ half to oxidize and support the electronic current by a relatively abundant population of holes, (b) the low-PO$_2$ half to reduce and support the electronic current by a relatively abundant population of electrons, and (c) the large PO$_2$ drop across (a) and (b) to support a mixed electron/hole current despite the very low local populations (hence conductivities) of electronic charge carriers at the V-shaped minimum in the Brower diagram.

In effect, the electrolyte in the above steady state behaves like a $p-n$ junction, the high-PO$_2$ half is the p-region, the low-PO$_2$ half is the n-region, and the V-shaped minimum in the conductivity of electrons and holes (set by when their populations are nearly equal in the Brouwer diagram) is the junction. Such a large and abrupt oxygen potential drop with an associated large and abrupt $E_F(x)$ increase, referred to as an oxygen-potential transition,[20] is expected in every good

electrolyte, and its magnitude and steepness increase with the current density and with increasing electrode overpotential. As the operating temperature of SOFC/SOEC is lowered, the electrode kinetics become more sluggish and the electrode overpotential must increase. This will drive toward a more extreme oxygen-potential transition. However, such a transition may take a longer time to develop because, at lower temperatures, the electronic/ionic mobilities are so slow that it is difficult to reach the steady state and local equilibrium: To establish a profile like in Figure 1c, there needs to be a long-range transport of charge-neutral O$_2$ inside the electrolyte, by transporting ions and electrons simultaneously. Note that, unlike the electronic $p-n$ diode, there is no significant space-charge region at the "junction" interface in the solid electrolyte. The sharp jump occurs in the part of the concentration-dependent chemical potential, not in the electrostatic potential.

The implication of the sharp log PO$_2$ or oxygen potential transition on damage development is profound. Despite the tiny magnitude of the electronic current, it serves as a "short-circuit" current that makes almost the entire oxygen-electrode half of the electrolyte experience the same oxygen potential of the oxygen electrode, and *vice versa* in the other half. Therefore, any oxidation-caused damage normally expected only at or near the oxygen-electrode/electrolyte interface now becomes possible throughout the entire oxygen-electrode half. Similarly extensive reduction-caused damages are also expected throughout the reduction/fuel-electrode half. This is schematically illustrated in Figure 1c comparing a sigmoidal vs a linear oxygen potential distribution assuming the same damage threshold set at a fixed oxygen potential. It is clear that the at-risk region is much wider when there is a sigmoidal potential. In particular, if the boundary oxygen potentials at electrode/electrolyte interfaces—determined by the sum of atmospheric potential and the electrode overpotential, the latter increasing with increasing current, decreasing temperature, decreasing electrode efficiency, and decreasing electrode's effective area and triple-phase-boundary density—are high enough, then the entire oxygen-electrode half of the electrolyte can be at risk.

The above expectation is supported by experimental observations. In SOEC, common degradations under a high oxygen potential are in the form of pressurized oxygen bubbles (precipitated from a disproportionation reaction of the peroxide group (O$_2$)$^{2-}$ in an oxidized electrolyte[22]). While they are most commonly seen at the oxygen electrode/electrolyte interface,
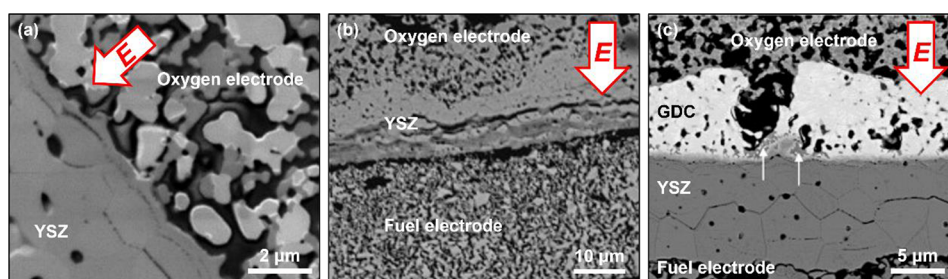
Figure 2. (a) Formation of oxygen bubbles preferentially at transverse grain boundaries and (b, c) in-plane (transverse) cracking inside the YSZ electrolyte after high-current-density SOEC operation. The dense electrolytes do not have grain boundary pores or cracks before cell operation. (a, b) Reproduced with permission from ref 10. Copyright 2011 Elsevier B.V. (c) Reproduced with permission from ref 11. Copyright 2012 Elsevier B.V.
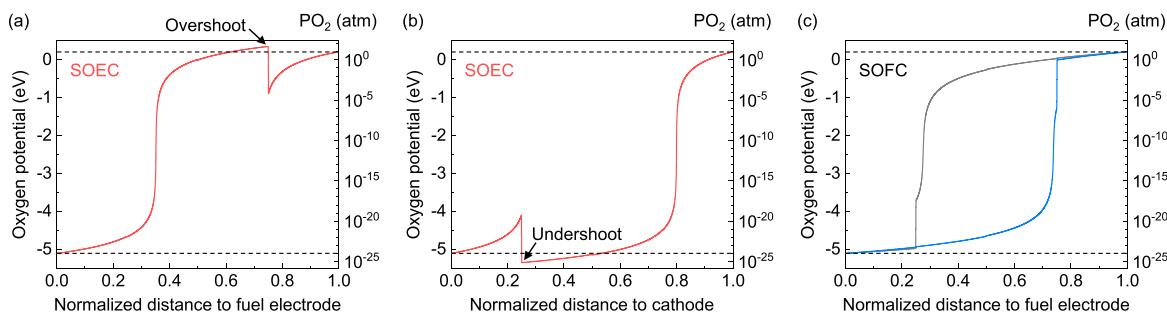

Figure 3. Calculated oxygen potential distribution inside a 10 μm-thick "polycrystalline" YSZ electrolyte under (a, b) SOEC (at -1 A/cm^2) and (c) SOFC (at 1 A/cm^2) modes at 800 °C. Three grain boundaries were equally spaced at 0.25, 0.5, and 0.75 normalized distances to the fuel electrode. One grain boundary—the one at 0.75 in (a) and the blue curve in (c), and the one at 0.25 in (b) and the gray curve in (c)—was assigned to be highly O^{2-} blocking (10^{-4} of the lattice O^{2-} conductivity), while others have 10^{-2} of the lattice O^{2-} conductivity. Boundary oxygen potentials were set as -5.1103 eV at the fuel electrode/electrolyte interface and 0.2129 eV at the oxygen electrode/electrolyte interface. Oxygen potential set as 0 eV at 1 atm oxygen partial pressure. For more details, please refer to Figures 3 and 4 in ref 25.

they have also been seen at grain boundaries well inside the electrolyte,[2,10,11,23] including ones in the midsection of the electrolyte far removed from the electrode/electrolyte interface (Figure 2a). Moreover, it was found that once the damage threshold is exceeded, which is certainly the case when oxygen bubbles already appeared, the bubble population shows a rather weak dependence on the distance to the oxygen electrode, which is consistent with the step-like profile of oxygen potential depicted for the oxidizing half in Figure 1a,c. As bubbles accumulate and grow, the cell degrades and cell impedance increases; eventually, they may lead to electrolyte cracking (Figure 2b,c) and catastrophic failure.[2,10] On the reducing half, reduction voids at grain boundaries and in the grain interiors have also been reported; once again they are consistent with Figure 1a,c in that their population has a weak dependence on the distance to the fuel electrode (see Figure 7 of ref 24).

As already mentioned, oxygen bubbles on grain boundaries are a common form of degradation inside SOEC electrolytes. Importantly, they preferentially form at transverse boundaries,[2,10] which also explains why they may eventually lead to in-plane cracking as shown in Figure 2b,c. Preferential formation of bubbles on grain boundaries may be attributed to heterogeneous nucleation (i.e., interfacial energy lowering the nucleation barrier) and/or a growth advantage (i.e., grain boundaries being fast diffusion paths), but if this is the case then bubbles should form on grain boundaries of all orientations. Therefore, there must be a thermodynamic advantage that favors transverse boundaries. In YSZ and in most other oxide ceramics, grain boundaries are electrically blocking (to electronic and/or ionic charge carriers) to various extent because of the presence of a Schottky barrier and/or space−charge effect. So, at the steady

state, an extra driving force in the oxygen potential is locally needed at the boundary to keep the current continuous across it. This translates to an oxygen potential jump across the transverse boundary[25] as shown in Figure 3a; there is no such jump at longitudinal boundaries because no current crosses them. It is such a potential jump that provides the additional thermodynamic driving force making transverse boundaries the favorable sites for bubble nucleation and stress-induced sliding/cracking. The same also applies to the low-PO_2 half where the oxygen potential dips across a transverse boundary in Figure 3b, which would favor the nucleation of reduction voids. Therefore, in addition to the step-like oxygen potential that serves to extend the spatial range of the electrode overpotentials to well inside the electrolyte, these potential jumps/dips at transverse grain boundaries (as well as other transversely blocking defects) further exacerbate the odds of damage nucleation throughout the electrolyte and make the transverse mode of degradation a leading cause of long-term damage in high-current-density SOECs. Similar degradation phenomena are also seen in SOFCs, though to a lesser extent. This is because (a) the electrode overpotentials are generally smaller in SOFC as we already pointed out before and (b) although the direction of the electronic leakage current is the same in SOFC and SOEC, the direction of the ionic current is opposite in the two devices, which makes overshoots, i.e., jumps and dips, of oxygen potentials at transverse boundary impossible in SOFC. This is shown in Figure 3c and further explained in ref 25.

A key consideration relevant to degradations is the interplay between redox potentials and stress fields. Oxidation and reduction (e.g., change of δ in $MO_{1\pm\delta}$ in a nominally 1:1 metal− oxide) of the solid electrolyte phase are accompanied by a

change in lattice parameters, which is known as chemical expansion/contraction. As a result, a synergistic effect of chemical potential distribution on stress distribution can arise. This is most relevant to ceria-based electrolytes that are known to suffer large volume expansions upon reduction.[26] (In contrast, the chemical expansion of zirconia-based electrolytes, though measurable—there is a slight contraction under reduction[27]—is practically negligible perhaps.) Physically, δ manifests itself as ionic disorder, e.g., oxgen vacancies in the electrolyte. The equilibrium (stress-free) lattice parameter $a^{eq}(\delta)$, oxygen potential $\mu_{O_2}(\delta) = const + k_B T \ln PO_2^{eq}(\delta)$ (obtained from the tangent extrapolation of Gibbs free energy curve of the solid electrolyte, $G(X_O = (1 \pm \delta)/(2 \pm \delta))$), the redox potential $E_F(\delta)$, and δ all have a one-to-one relationship with each other. A large stress buildup, compressive on the reduced half and tensile on the oxidized half, is thus expected, especially when the oxygen potential $\mu_{O_2}(\delta)$ transition is abrupt and large (which means the $a^{eq}(\delta)$ transition is abrupt and large). In addition, at the outer (lateral) edge of an electrolyte membrane subject to the potential transition, hence, the tension/compression transition, there is a stress concentration that can nucleate cracks that veer into the tensile side (the oxidized side in a ceria) of the electrolyte after propagating inward a short initial distance along the transition boundary. This is thus a mode of longitudinal degradation, and it tends to proceed very fast once the crack forms. Consistent with the above stress analysis of the origin of crack formation and crack location/direction, catastrophic cell failures were reported for high-current-density SOEC with a trilayer GDC/zirconia/GDC electrolyte operated at below 750 °C and were attributed to longitudinal cracking from the fuel electrode/electrolyte interface toward the air electrode.[28]

2.2. Strategies to Mitigate Damage. The almost step-like oxygen potential profile and its overshoots at ion-blocking transverse boundaries provide an important lesson: It is not prudent to assume that the redox potential in the electrolyte is a linear interpolation between electrode potentials. In fact, it is not prudent to assume even "oxygen pressure inside the electrolyte will *never* become higher than the pressure corresponding to the electrode potential of the oxygen electrode and *never* lower than corresponding to the electrode potential of the hydrogen electrode, irrespective of which mode or condition for the cell operation",[19] as there are certainly such violations in Figure 3a,b at transverse boundaries. On the other hand, knowing the origin of these unexpected high and spatially extended oxygen potentials, one can now design better materials and follow better practice to mitigate damage.

Some strategies are already known, chief among them being the following: (1) Improve the electrode efficiency and electrode–electrolyte contact to lower the electrode over-potential, which can extend well inside the electrolyte especially when the magnitude of the overpotential is large. Likewise, lowering the resistance of internal interfaces (such as buffer layers) by better wetting will lower the overall potential under the same current density, thus lowering the risk of internal damage. For example, a pulsed-laser deposited (PLD) $PrBa_{0.5}Sr_{0.5}Co_{1.5}Fe_{0.5}O_{5+\delta}$ interlayer has been reported to improve the contact between the protonic electrolyte $BaZr_{0.4}Ce_{0.4}Y_{0.1}Yb_{0.1}O_{3-\delta}$ and the cathode $PrBa_{0.5}Sr_{0.5}Co_{1.5}Fe_{0.5}O_{5+\delta}$, which lowers the ohmic and polar-ization resistances and improves the stability of the cell.[29] (2) Develop columnar grain structure with mostly transverse grain

boundaries to remove ionic bottleneck, which would lower the cell resistance, increase the efficiency, and improve the stability. For example, epitaxially oriented PLD $BaZr_{0.8}Y_{0.2}O_{3-\delta}$ films have been demonstrated to be an excellent proton conductor.[30] (3) Periodically include some brief periods of the SOFC mode during a prolonged SOEC operation to reverse the ion flow, hence lowering and reversing the excessively high potential distribution and possibly even reversing oxygen-bubble nucleation/growth. As these processes will take time to rebuild, some "safety window" may thus be provided.[2,25]

Beyond these measures, tuning electronic conduction provides another fundamental solution. This is because the root cause of the step-like oxygen pressure transition is the V-shaped minimum in electronic conductivity; thus, smoothing the minimum and increasing the minimal electronic con-ductivity, which can be achieved by minute doping of the electrolyte, will fundamentally smooth out the oxygen potential transition and the magnitude of the attendant overshoots.[25] (We are of the opinion that the electronic conductivity of YSZ in multilayer SOFC/SOEC electrolytes is too low, and its damage tolerance may be improved by a slight increase of the electronic conductivity.) Moreover, taking advantage of solute segregation, one can selectively dope grain boundaries to modify their space charge, Schottky barrier, and electron and hole conductivity, which will influence not only the potential overshoots there but also the entire potential distribution throughout the electrolyte because of its effect on overall steady-state electric current density.

As mentioned before, residual stresses may arise from chemical expansion/contraction, and in layered structures, different chemistries and thermal expansion coefficients may make matters worse. Such residual stresses and stress concentrations cannot be avoided in a standard electrolyte configuration that is compositionally uniform and geometrically flat. However, a graded composition may help smooth out the stress gradient and, thus, lessen stress concentrations. Another approach is to use a wavy interlayer or undulating composition, which is known to limit the spatial range of the stress concentration to the scale of the wavelength, and on fracture energy ground, a short enough undulation wavelength will make crack nucleation no longer possible.[31,32] This combined geometric/compositional solution is recommended for electro-lytes that suffer large chemical expansions. The same geometric/compositional solution outlined above is also effective for mitigating cracking at multilayer interfaces, such as ones observed in a trilayer GDC/zirconia/GDC electrolyte men-tioned above.[28] (The same chemical expansion should also arise at transverse grain boundaries with oxygen potential over-shoots/jumps. However, since grains in a typical electrolyte are usually 2−10 times smaller than the membrane thickness, by itself the stress range at grain boundaries may not be long enough to initiate cracking.)

One should also be cognizant of the possibility of interface embrittlement caused by electrochemical loading via chemical/structural weakening due to, e.g., solute segregation or electrolytic changes to interfacial bonding. (Under a large ionic current, nonequilibrium solute segregation may become appreciable due to the ion−solute coupling.) For example, we recently observed a fracture-mode transition in a high-current-density PCEC electrolyte, $BaZr_{0.1}Ce_{0.7}Y_{0.1}Yb_{0.1}O_{3-\delta}$, from intragranular fracture before testing to intergranular fracture after testing, at all boundaries regardless of orientations.[33] (See Supplementary Figure S13 of ref 33.) Another possibility is

electrolytically enhanced grain boundary corrosion. For example, in direct carbon fuel cells with liquid metallic antimony anodes (the anodic reactions being $2Sb + 3O^{2-} = Sb_2O_3 + 6e^-$ and $C + 2Sb_2O_3 = 3CO_2 + 6Sb$), antimony corrosion of the YSZ and GDC electrolytes along grain boundaries of all orientations was reported; no corrosion was seen in single-crystal YSZ electrolyte.[34] Again, compositional engineering at the interface and smoothing of current concentrations, as well as avoidance or a better control of embrittling impurities, may be needed.

Lastly, we emphasize that the above strategies should be practiced holistically. For example, strategies that enhance cell performance, say by using more efficient electrodes, may inadvertently introduce a new source of degradation as illustrated below. Several engineering designs of bilayer/multilayer electrolytes have proved effective for enhancing SOFC/SOEC performance. One approach uses a bilayer YSZ/GDC electrolyte to suppress chemical reactions that would otherwise occur, forming insulating $SrZrO_3$ and $La_2Zr_2O_7$ between a single-layer YSZ electrolyte and oxygen electrode.[35] Meanwhile, a bilayer $GDC/Er_{0.4}Bi_{1.6}O_3$ electrolyte can utilize the high O^{2-} conductivity of $Er_{0.4}Bi_{1.6}O_3$ without subjecting it to low oxygen potentials that would cause $Er_{0.4}Bi_{1.6}O_3$ to decompose,[36] and a trilayer GDC/zirconia/GDC electrolyte can utilize the high O^{2-} conductivity of GDC while still blocking the electronic (electron) leakage of GDC.[35] Although these structures can enhance cell performance, they may suffer unintended degradation because layer interfaces being phase boundaries are more likely than not ionically blocking, which makes them prone to oxygen potential overshoots, thus nucleating damage.[37,38] Oxygen-bubble formation and in-plane cracking/delamination were indeed observed at such interfaces, although one cannot rule out the possibility that they were due to mismatched thermal/chemical expansion coefficients or a weak interfacial strength (which implies a high interfacial energy, thus lowering the barrier for bubble nucleation.) Therefore, performance-enhancing layer designs need to incorporate additional interface engineering described earlier to deliver a holistic improvement.

To summarize, transverse degradation is the main degradation mode for SOFC/SOEC electrolytes. It mostly occurs in high-current-density operations and/or prolonged SOEC service lives, as it is a gradual degradation mode that proceeds by the nucleation and growth of oxygen bubbles or reduction voids with an initially slow damage accumulation. Given enough time, however, it may reach an advanced stage when bubble/void coalescence and linkage take hold that will soon lead to in-plane cracking, resulting in rapid crack propagation and catastrophic failure. Fast longitudinal degradation is less common in SOFCs and SOECs, although it could arise from stress-nucleated cracking due to redox forces if the operating conditions become much more severe than the ones used today (OCV $\sim$ 1.1 V for H_2−SOFC at 800 °C). This can be particularly problematic at lower temperatures when stress relaxation and crack blunting/healing are less effective, as already seen in the catastrophic failure of a SOEC with a trilayer GDC/zirconia/GDC electrolyte.[28]

3. SOLID-STATE ALKALI METAL BATTERIES

3.1. Overview of Damage Mechanisms. Similar degradation modes are expected in solid electrolytes in solid-state metal batteries. While most commercial rechargeable metal batteries use liquid electrolytes, all-solid-state lithium metal batteries are under rapid development and may enter some

markets soon. Having a high-energy-density lithium metal anode and no flammable organic liquid electrolyte, these new batteries hold the promise of better performance and safety. Ceramic solid electrolytes under investigation include oxides, sulfides, and halides, and a variety of degradation phenomena are already well-known. Historically, in rechargeable batteries ceramic solid electrolytes first appeared in Na−S batteries operating at 300 °C; they were from a family of Na/beta-alumina ceramics, and they too suffered from degradation. Below, we will apply our synopsis of SOFC/SOEC degradation to anticipate the degradation modes in solid electrolytes in metal batteries. We will next conduct a "failure analysis" in several case studies to better understand the phenomenology.

Our synopsis of SOFC/SOEC makes it clear that a fundamental cause of electrode degradation is the unexpectedly high, abrupt, and spatially extended oxygen potential distribution inside the oxide electrolyte, which originates from the (slightly) mixed conducting nature of the electrolyte. This can be further exacerbated at kinetic bottlenecks, transverse grain boundaries in particular, but also at residual pores and cracks. When chemical expansion/contraction is present, the abruptness of the potential distribution also gives rise to a stress distribution and stress concentrations at the locale of the transition where $\nabla \mu_{O_2}(\delta(\mathbf{x}))$ is the largest. The excessive potential can cause oxygen accumulation forming oxygen bubbles or oxygen depletion forming reduction voids, and the stress concentrations can nucleate cracks that may further grow by accumulating oxygen bubbles. Logically, the same reasoning applies to solid electrolytes in metal batteries. (a) There is always some minute electronic conduction in a solid electrolyte, and their inherent redox dependence favoring electron conduction on the reducing side and hole conduction on the oxidizing side will necessarily result in a V-shaped minimum in the electronic conductivity in a mid-$PO_2^{eq}(\delta)/E_F(\delta)$ point in the Brouwer diagram as depicted in Figure 1b. (b) Since Figure 1a follows Figure 1b, there must be a steep, sigmoidal, or even step-function-like distribution of redox potential (which has an electrostatic term that all ions/electrons/holes see, plus a chemical-potential contribution that depends on the electron/hole concentrations) incorporating all the electrode overpotentials (on top of the extremely reducing metal anodes and oxidizing high-voltage cathodes)—developed in the solid electrolyte. (c) Whereas the redox potential E_F in SOFC/SOEC pertains to oxygen partial pressure, the redox potential E_F in metal batteries pertains to the equivalent chemical potential of the electrode metal, e.g., Na or Li. Therefore, just like oxygen bubbles are expected in high oxygen potentials in SOFC/SOEC, Na or Li metal precipitates are expected in high Na/Li chemical potentials in Na/Li batteries. These precipitates, often named "dendrites", have already been widely reported since the early days of Na−S batteries, and their reporting continues through the recent development of all-solid-state Li batteries.[6−9] (d) At transverse grain boundaries that are ionic bottlenecks, a higher electrostatic-potential drop can build up. In a good electrolyte that has a high though nearly fixed concentration of ionic charge carriers, this electrostatic potential drop translates to a redox-potential jump, as depicted in Figure 1c, which further exacerbates the potential excess making transverse boundaries the preferred sites of Na/Li precipitation. This, too, has been observed since the early days of Na−S batteries through the recent development of all-solid-state lithium metal batteries.[6,9,39,40] (e) The redox of solid electrolytes causes a
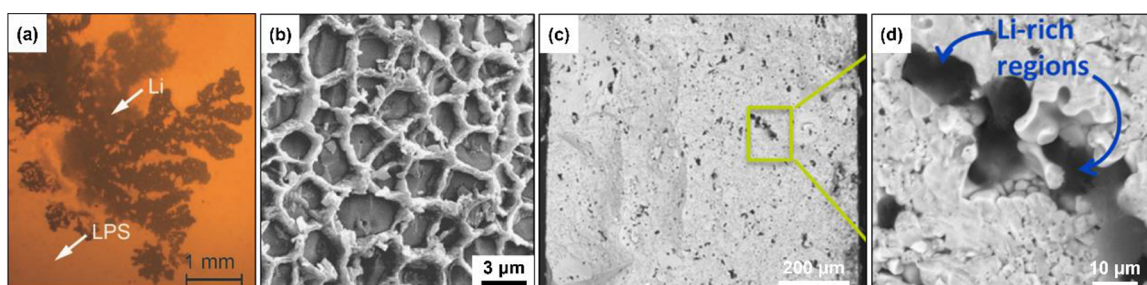
Figure 4. (a) Lithium penetration through the polycrystalline β-Li_3PS_4 electrolyte. (b) Lithium "web" formation at grain boundaries of polycrystalline $Li_{6.25}Al_{0.25}La_3Zr_2O_{12}$ electrolyte. (c, d) Lithium precipitation inside closed pores (dark spots) in polycrystalline $Li_7La_{2.75}Ca_{0.25}Zr_{1.75}Nb_{0.25}O_{12}$ electrolyte. (a) Reproduced with permission from ref 41. Copyright 2017 Wiley-VCH Verlag GmbH & Co. KGaA, Weinheim. (b) Reproduced with permission from ref 48. Copyright 2016 Elsevier Ltd. (c, d) Reproduced with permission from ref 9. Copyright 2017 American Chemical Society.

synergistic change in the equilibrium (stress-free) lattice parameter distribution $a^{eq}(\delta(\mathbf{x}))$, referred to as chemical expansion/contraction before, hence an elastic strain distribution that mirrors the redox potential distribution $E_F(\delta(\mathbf{x}))$. Since the overall internal stress must add up to zero, the oxidized side and the reduced side must have opposite stresses with a stress concentration at the outer edges of their junction. Stress-induced electrolyte cracking has also been observed in metal batteries, and we will cite the literature after further analysis.

While the above establishes the analogy between SOFC/SOEC and metal batteries, there are important differences between them. (i) Metal batteries operating at ambient temperatures are likely to have a much lower electronic conductivity than SOFC/SOEC operating at >600 °C. Since the abruptness of the redox potential distribution $E_F(\delta(\mathbf{x}))$ comes from the need to maintain local equilibrium, which must involve electronic conduction, the steady state and, hence, the abrupt potential distribution will take more time to establish. (The initial state of the redox potential in the electrolyte is flat and identical to that seen in a virgin battery, with abrupt jumps to match the electrode's redox potentials at electrolyte/electrode interfaces. From this state, it will gradually evolve into the steady state.) Therefore, the incubation time before redox-induced degradation develops may be quite long in metal batteries. In fact, during fast charging/discharging, the steady state may never be established, which poses a problem for using accelerated tests to simulate degradation development in metal batteries. (ii) In contrast to (i), the slow kinetics at ambient temperatures may severely limit the electrode efficiency, thus necessitating an extreme overpotential, which will be carried over into the electrolyte as already described by (b) in our reasoning above. This will lead to a more severe redox-induced degradation. An example is batteries operated at frigid temperatures; they tend to degrade faster. (iii) Extreme operating conditions such as high current densities and high electrode potentials may encroach the electrolytic window, thus increasing electronic conduction and hastening the development of the steady-state shock-like profile in (i). (iv) In ceramics, metal nucleation is much easier than oxygen-bubble nucleation because cation-to-metal transformation does not entail a huge volume expansion as in anion–gas transformation (e.g., oxygen evolution reaction typically entails a large kinetic overpotential); in addition, the metal–ceramic interface is likely to be less energetic than the gas–ceramic interface, both decreasing the nucleation barrier of metal precipitation. This applies to both transverse degradation and longitudinal degradation. (Longitudinal degradation in metal batteries mostly involves metal dendrites instead of longitudinal cracking,

which is the case in SOFC/SOEC and has the same issue of crack nucleation as for bubble nucleation.) As will be explained below, longitudinal dendrites have been widely observed since the early days of Na–S batteries through the recent development of all-solid-state batteries;[6,39,41−43] this is in contrast to the rare occurrence of longitudinal cracking in SOFC/SOEC. As a result of the frequent occurrence of longitudinal degradation, mode coupling between longitudinal and transverse degradation also becomes much more frequent in metal batteries, which is elaborated below. (v) Metal precipitation causes a volume expansion locally, which leaves a residual compressive stress on the reduced half of the solid electrolyte. In analogy to chemical expansion, this will induce a residual tensile stress on the oxidized half, setting up stress concentration in the midsection between them. This is another example of the synergistic effect of chemical potential distribution on stress distribution. Later, we will analyze a recent example of spallation cracking in a Li_5PS_5Cl electrolyte (see case (D) below) which belongs to this case.[39] But we will also analyze a more complicated (and more interesting) stress distribution that causes circumferential cracking in doped $Li_7La_3Zr_2O_{12}$ (see case (E) below).[40] Similar cases are seen in plate-like metal coating at grain boundaries generating stress concentrations at and near their edges that can cause further microcracking, often to fall on grain boundaries as well.[6] Indeed, metal plating into a crack can generate additional stress concentrations in front of the crack tip, providing the driving force for the crack to propagate (or more cracks to nucleate) ahead of metal filling. This form of cracking, called displacement-controlled Mode-I cracking in fracture mechanics, is an observation that was emphasized in several studies.[39,40]

3.1.1. Case Studies. (A) In the Na–S batteries studied by De Jonghe et al.[6,7] in 1981, Na/beta-alumina solid electrolytes showed longitudinal degradation in the form of Na dendrites, which filled a Na-filled crack and propagated rapidly through the solid electrolyte, leading to short-circuiting and immediate failure (called mode I—unrelated to the classification in fracture mechanics mentioned above—by De Jonghe et al.[6,7]) They also showed transverse degradation in the form of slow internal deposition of Na metal islands inside the solid electrolyte, which increased the electronic conductivity of the electrolyte and caused electronic leakage and self-discharge (De Jonghe et al. called it mode II, again unrelated to the classification in fracture mechanics). Importantly, as shown by Figure 3 of ref 6, there is a sharp, planar boundary between the reduced regime with precipitated metallic Na and the unreduced regime, and the boundary moved from Na electrode to S electrode after extended cycling (i.e., with more transferred charge). These are the essential features for slow yet progressing transverse
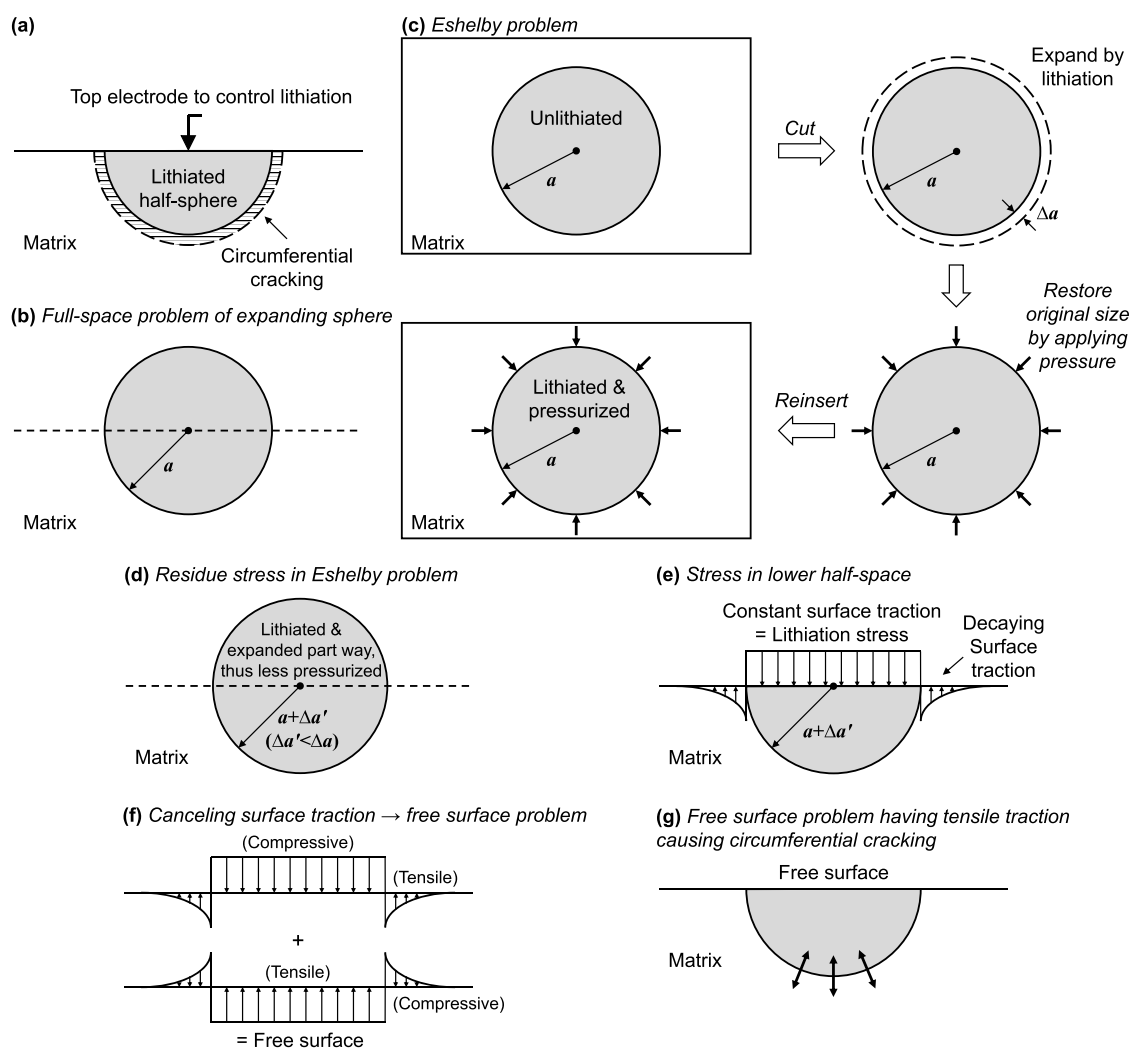
Figure 5. Lithiation and stress analysis using Eshelby's gedanken experiment. (a) Experimental setup using a point electrode to lithiate radially in a half-sphere. (b) Equivalent full-space problem with the point current source at the center. (c) Eshelby problem of misfitting inclusion of the enlarged, lithiated sphere. It can be made to fit again by applying a uniform, compressive surface traction. (d) When the perfectly fitting but compressed sphere is allowed to relax in the matrix by removing the (internal) surface traction, it expands part way but still under some pressure. (e) Surface traction on the equatorial half-plane viewed in a free-body diagram, which maintains the same stress state in the lower half-space as in (e). (f) Surface traction in the above free-body diagram is canceled out by applying an opposite surface traction, making the surface traction-free, hence back to the same experimental state as in (a). (g) Radial tension left at the bottom boundary of the lithiated half-sphere is the cause of circumferential cracking.

degradation despite the concurrent presence of longitudinal dendrites. The metallic Na precipitates at grain boundaries also caused grain-boundary microcracking, which can be coupled to longitudinal degradation and initiate out-of-plane cracks, as is the case seen in all-solid-state lithium metal batteries.[39]

(B) In all-solid-state lithium metal batteries, the short-circuiting event takes place rapidly, once some threshold current density, known as the critical current density (more on this in (D)), is exceeded. Above the critical current density, rapid lithium growth/penetration across the solid electrolyte is filamentary in nature and follows the direction of the electric field[41−43] (Figure 4a; also see Figure 1 and Supplementary Video S1 of ref 43). This makes it a longitudinal mode of degradation. The above event is likely mediated by metal plating, which nucleates an initial crack, followed by additional metal plating in the crack to build up a large enough stress concentration that leads to the formation of the final, short-circuiting, metal-plated crack. In this connection, the critical current density is likely correlated to the critical stress intensity

factor, K_{IC}, in fracture mechanics, which is a material property specifying the fracture toughness of the material. Note that the critical current density reported is typically the nominal density, so the local current density at the electrode/electrolyte interface, which is usually porous, should be higher. This points to the importance of good wetting at the metal-anode/solid-electrolyte interface.[4,44−46] Poor interfacial wetting, either due to intrinsic materials properties or unintentional/unattended surface contamination, will decrease the true contact area,[45] increase the overpotential, and cause electric field/current concentrations, thus leading to larger impedance, lower (nominal) critical current density, and faster cell failure.

(C) Because metal precipitates are like virtual electrodes and can generate electric field/current concentrations, which alter and concentrate the redox potentials that cause further metal precipitation and stress concentrations, mode coupling is much more common in solid electrolytes in metal batteries than in SOFC/SOEC. This is especially true when metallic phases precipitate out on grain boundaries because of the proximity of

neighboring boundaries and the propensity of metal precipitation on them. For example, a three-dimensional lithium "web" decorating the grain boundary network (Figure 4b) was seen in (doped) $Li_7La_3Zr_2O_{12}$ electrolytes.[47−49] Such a web could develop in the following way: Li dendrites grow from the metal electrode along longitudinal boundaries first, and the field concentrations at their three/four-grain junctions cause plating of the transverse boundaries between them. Alternatively, internal precipitation of metallic Li triggered by the high Li potential occurs at transverse boundaries first, and the lowered impedance and the field concentrations at their three/four-grain junctions cause electrical plating of the (longitudinal) boundaries between them. Note that initial internal precipitation and/or filament nucleation from the electrode/electrolyte interface is likely to occur at interface asperities and/or residue pores nearby (Figure 4c,d for lithium-filled closed pores inside the solid electrolytes).[9,50] This could pose a difficult problem for engineers: a rough surface is often needed to promote electrode adhesion, yet it may provide uncommonly favorable sites for metal precipitation, and internal pores may be very difficult to remove completely in processing/sintering while trying to maintain the optimal chemistry and microstructure.

(D) Because of metal insertion, the initial internal precipitation or filament nucleation at the electrode/electrolyte interface will immediately generate a stress concentration locally. Such stress concentration is most acute at any compositional discontinuity. For example, in ref 39, at the edge of lithium plating or the planar reduction front defined by the edge of the contact Li/Na-metal electrode, electrode (Li_5PS_5Cl, Na-beta-alumina, Li_3N) "spallation" (along with chipping, see their Figure S3) was observed, leaving a short longitudinal crack behind (though the authors of ref 39 called it a "vertical crack" or "transverse crack"). Next, the short crack was coated by Li/Na, and a virtual electrode formed there. Third, the above process first occurring at the electrode/electrolyte interface is repeated at this new locale—the crack tip—where there is an electric field/current concentration, thus renewing the process of forming and extending a filamentary Li/Na dendrite. Fourth, mechanically, once a long enough dendrite is formed, Li/Na plating along the dendrite, working like a thickening wedge, can provide the requisite stress concentration to pry open the crack further, which opens a section of fresh crack without any Li/Na plating; the new section is capable of receiving metal plating. (This is crack displacement-controlled Mode-I cracking in fracture mechanics, mentioned before.) Fifth, as this process continues, eventually, the crack length becomes sufficiently long and the Li/Na plating in its wake sufficiently thick, so much so that the stress intensity factor (K_I) reaches K_{IC} and the fracture toughness (a material property) of the electrolyte is overcome, leading to a sudden rapid propagation of the crack. If the electrolyte is thick enough, the crack under the displacement control will eventually "run out of steam" and stop. This happens when it has extended far enough so that the crack tip no longer provides a high-stress region, and the stress intensity is no longer above critical (i.e., K_I now falls below K_{IC}). Sixth, over time, this crack will itself be coated by Li/Na to increase the crack-face displacement and turn into a more fully grown dendrite, which increases the stress intensity again to cause more crack propagation, and the process will repeat itself during charge/discharge cycles until the cell fails.

(E) The interplay of metal plating or metal internal precipitation, stress concentration, cracking, and dendrite is next analyzed using another geometry. The study of ref 40 of Li

deposition and cracking in a doped $Li_7La_3Zr_2O_{12}$ solid electrolyte utilized a point electrode, which generates a radial field causing Li penetration and/or internal precipitation inside a half-sphere as schematically depicted in Figure 5a. The stress state inside and at the edge of the half-sphere can be analyzed using Eshelby's "gedanken" experiment as follows. First, consider a full-space problem, including a full-sphere that is to be lithiated by a point source at the center (Figure 5b). Second, lithiate the sphere, which enlarges it radially, but also apply a uniform, compressive surface traction to force the sphere back to the original size to maintain the fit (Figure 5c). Third, release the (internal) surface traction and let go of the sphere, which will expand. However, because of the elastic constraint of the surrounding, the expansion will stop before reaching the fully lithiated size, leaving the sphere again in a pressurized state (though less so than in Figure 5c). Meanwhile, its surrounding also experiences a radial pressure but a tangential tension, although their magnitude will decay with the radial distance (Figure 5d). Fourth, on the equatorial plane of the full-space (corresponding to the surface of the lower half-space), the only surface traction is one normal to the surface, and it is uniformly compressive on the sphere and tensile though radially decaying around the sphere (Figure 5e, which is called a free-body diagram in mechanics). Fifth, to cancel the above surface traction, add an opposite set of normal traction—tensile on the sphere and compressive though radially decaying around the sphere (Figure 5f), leaving the equatorial planar surface traction-free. Six, now that the (lower) half-space has a "free" surface, it can be removed from the other (upper) half-space, and its stress state exactly corresponds to what is obtained by lithiation in the actual experiment of Figure 5a. Because the surface tensile traction in the center of Figure 5f tries to pull the half-sphere away from the lower half-space, there is a maximal Mode-I stress intensity factor K_I at the bottom of the half-sphere; see Figure 5g. (There is also a Mode-II stress intensity factor K_{II} at the upper (surface) edge of the half-sphere.) This maximal K_I is proportional to the product of the square root of the half-sphere radius and the lithiation stress, namely, the pressure in Figure 5d, same as the normal traction in Figure 5e,f. Eventually, as lithiation continues and the half-sphere grows large enough, this maximal K_I will reach K_{IC}, and cracking is initiated at the bottom and goes around the half-sphere, forming a circumferential crack. (The situation here is analogous to indentation cracking of ceramics, in which the circumferential crack, called lateral crack, develops not during indentation, i.e., loading, but upon indent removal, i.e., unloading.) Circumferential cracking around a lithiated half-sphere was observed in ref 40. It is also interesting to note three other events. First, as lithiation proceeds without cracking, the stress will build up continuously until it reaches the critical stress for Li extrusion, which appears as Li metal fingers growing out of the solid electrolyte as observed in ref 40. (The extrusion stress is proportional to the deformation resistance, i.e., the yield stress, of Li, but it is higher by a factor of about 3 or more because of the multiaxial nature of the extrusion process and the friction encountered during extrusion.) Second, once cracking occurs, the lithiation stress is relieved; hence, extrusion stops, which was also observed in ref 40. Third, the circumferential crack is initially "clean", without any Li. However, since it is a transverse boundary blocking the electric current, it will begin to accumulate Li, which was also observed in ref 40.

3.2. Strategies to Mitigate Damage. The above case studies make it clear that, in order to improve the integrity of

metal batteries, it is important to improve the chemical, microstructural, and ultimately electric-transport uniformity inside the solid electrolyte, which will minimize kinetic bottlenecks, the number of nucleation sites for metal coating/precipitation, and stress concentrations.[51−55] Toward this end, for the bulk solid electrolyte, one would generally prefer electrolyte materials with a wider electrochemical stability window, better processability/sinterability, and higher mechanical robustness. High density and a uniform microstructure with few pores or other macroscopic defects are crucial to avoid blocking sites of ion transport, preferential sites for early stage metal precipitation and later-stage degradations, and stress concentrators that initiate mechanical damage. Grain-size uniformity is another important factor that has not been adequately addressed in the literature. It matters because abnormally large grains are again preferential sites for degradation. Moreover, they are often related to in-grain pores, which break away from fast-growing grain boundaries during sintering, and once detached they lose access to grain-boundary diffusion, thus becoming very difficult to sinter further.[56] In general, a higher fracture toughness, e.g., imparted by transformation toughening,[57] is beneficial. The addition of second-phase particles of tetragonal (such as yttria-stabilized) zirconia has been demonstrated to transformation-toughen beta-alumina electrolyte in Na−S batteries.[58] However, it should be noted that thermodynamically the transformation toughness will decrease with increasing temperature as the tetragonal phase becomes more stable and, thus, less susceptible to stress-assisted transformation.[59] Another side effect of adding zirconia particles comes from boundary pinning, which homogenizes the microstructure,[60] which has been recently shown to improve interfacial wetting between beta alumina and sodium metal in Na−S batteries.[61] Appropriate doping to expressly tune the space charge at grain boundaries[62] in order to control grain growth and to minimize the potential jumps at these bottlenecks is also an approach that should be beneficial. Lastly, since Li and Na are volatile during high-temperature processing, it is critical to minimize or (by compositional design) allow for their loss in order to maintain the intended stoichiometry of the solid electrolyte. This can be done, for example, by introducing an excess-Li source such as Li_3N.[63]

Microstructure design goes beyond a monolithic electrolyte layer. One promising design is to construct, from a monolithic solid electrolyte, a porous/dense/porous structure that transitions the two electrodes with an electrolyte layer, the dense layer, between them. This dense layer, (a), has a very thin effective electrolyte thickness and is in intimate contact with the metal anode, (b), and the Li cathode, (c), because both metal and Li can respectively penetrate the two porous layers (b, c) on their sides. As a result of the thin thickness of (a) and a very large effective contact area between (a) and (b) and between (a) and (c), faster transport kinetics (thus higher current densities) is readily achieved. Yet the battery is overall robust despite the very thin electrolyte (a) because (a) is bonded to and, thus, mechanically supported/protected by (b) and (c) on two sides.[64,65]

Not surprisingly, ensuring a good contact between the metallic anode and the solid electrolyte has been known to be important, and stack pressure has been applied toward this end of increasing the true contact area. But its application to large-scale practical cells remains problematic. In fact, the fundamental problem lies not only in mechanical contact but also in nanoscale wetting at the metal−electrolyte interface, which must be maintained over a large area. In materials engineering, one well-known approach to solving this kind of interfacial contact problem is surface modifications.[33] Recently, it was demonstrated that ALD Al_2O_3 can react with Li metal to substantially lower the contact resistance of ($Li_7La_{2.75}Ca_{0.25}Zr_{1.75}Nb_{0.25}O_{12}$ or LLCZN) garnet electrolyte/Li electrode.[4]

There are other examples of interfacial modifications by thin-film techniques. First, thin-film Li^+ solid electrolyte LiPON prepared by sputtering Li_3PO_4 in N_2 is known to have exceptional stability and extended cycle life.[66] Second, as mentioned before, highly textured PLD films of $BaZr_{0.8}Y_{0.2}O_{3−\delta}$ can enhance protonic conductivity.[30] Third, the PLD $PrBa_{0.5}Sr_{0.5}Co_{1.5}Fe_{0.5}O_{5+\delta}$ interlayer can improve the contact between $BaZr_{0.4}Ce_{0.4}Y_{0.1}Yb_{0.1}O_{3−\delta}$, a protonic electrolyte, and the cathode.[29] Fourth, maintaining a good stoichiometry of PLD $Li_{6.25}Al_{0.25}La_3Zr_2O_{12}$ has been reported to enable high ionic conductivity in thin-film-type Li−garnet electrolyte.[63] Lastly, in addition to being of use for surface modification, thin-film electrolytes in thin-film electrochemical cells may be of interest. For example, a thin film YSZ electrolyte can allow SOFC to operate at as low as 300 °C.[67]

While the above strategies of interfacial engineering are promising, it could still be challenging to ensure good interfacial properties, such as wetting, throughout the battery lifetime, which must endure electrochemical cycling. The concern is whether cell degradation will ensue and rapidly progress to failure once some loss of contact has started. Some lessons may be drawn from dielectric breakdown, which has been well studied (more on this later). Because of the current concentration, the local current density will dramatically increase at the worst contact point, which leads to its failure; after that, the current concentration shifts to the next worst contact points nearby, and the above event repeats there. Once initiated, this chain reaction generally propagates very fast and is known to lead to very rapid device failures. This could well be the case in metal batteries.

4. FIELD ASSISTED CERAMIC PROCESSING

Several densification techniques have been developed to implement high throughput porosity reduction of ceramic compacts using an electric or electromagnetic field, thus achieving rapid heating and sintering. Spark plasma sintering (though no spark actually exists) is one such technique, in which a modest voltage (∼10 V) drives a large electric current to pass through a set of electronically conductive graphite dies within which a ceramic compact is electrically heated and mechanically compressed at the same time. As most of the current bypasses the much less conductive ceramic, the current flowing through the sample and the resultant Joule heating are not large. But contact heating is already so intense that complete densification can be achieved within seconds thanks to mechanical consolidation at high temperatures. A pressureless version of the above is the so-called flash sintering technique,[68] in which the ceramic compact sees no die pressure but is under a constant voltage (which is very large in some studies[69]) while the furnace temperature is being ramped up. As the ceramic conductivity increases with temperature, at some point the Joule heating will exceed furnace heating and a positive feedback loop of increasing temperature and Joule heating is entered under a constant voltage. This triggers a thermal runaway,[70−72] and once again full densification can be achieved within seconds. Clear evidence of electrochemical effects has been seen in samples
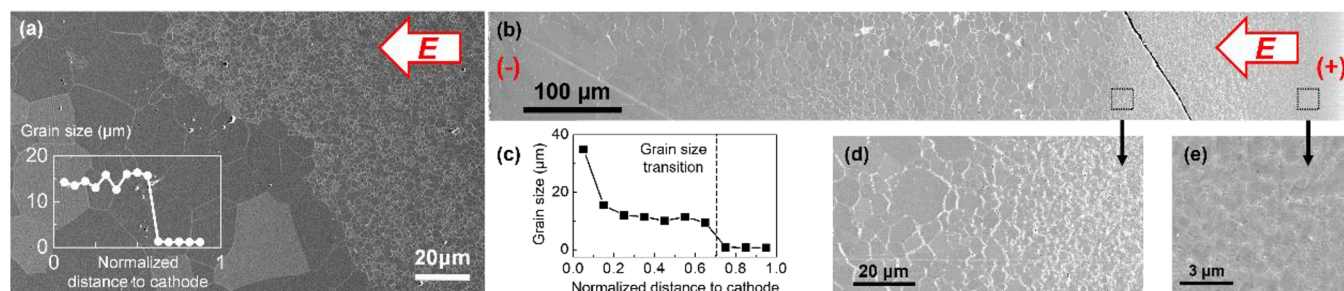
Figure 6. (a) Microstructure of cubic YSZ after high-temperature DC-electrical loading. Inset of (a): Measured grain size distribution of (a) as a function of normalized distance to the cathode. (b) Microstructure of tetragonal YSZ after high-temperature DC-electrical loading. (c) Measured grain size of (b) as a function of normalized distance to the cathode. High-magnification images show (d) the transition region and (e) the anode side. (a) Reproduced with permission from ref 20. Copyright 2018 Acta Materialia Inc. Published by Elsevier Ltd. (b–e) Reproduced with permission from ref 74. Copyright 2017 The American Ceramic Society.

prepared by these techniques, and the best examples came from flash sintering in which a microstructure gradient in the current direction is a common observation, seen, for example, in cubic YSZ,[73] tetragonal YSZ,[74,75] ZnO,[72,76] and TiO$_2$.[77] A much larger grain size was found on the cathode side in cubic YSZ, and the grain-size transition can be astonishingly sharp (Figure 6a),[20,73] suggestive of a solid-state electrochemical shock front. Since it is known that grain growth in zirconia (and several other similarly structured oxides) is faster under reducing conditions, the above grain-size transition provides direct evidence of the sharp oxygen potential $\mu_{O_2}(\delta(\mathbf{x})) = \text{const} + k_B T \ln PO_2^{eq}(\delta(\mathbf{x}))$ transition depicted in Figure 1a and discussed in Section 2. (These data also provided evidence for an association of electron and hole polarons with lattice oxygens and vacancies, which can be strong under extreme reducing and oxidizing conditions.[20]) The same observation made in tetragonal YSZ[74] (Figure 6b–e) provided even more definitive proof of the PO_2^{eq}/E_F transition. This is because in this ceramic the grain boundary mobility is controlled by (cation) solute drag that involves lattice diffusion,[62] and any enhanced grain growth must be mediated by a significantly enhanced cation mobility in the lattice. Therefore, the grain-size transition implicates an abrupt transition of the lattice mobility of cations, which can only come from an abrupt transition in $PO_2^{eq}(\delta)/E_F(\delta)$.

The analogy with the oxygen potential transition is apt not only for zirconia but also for GDC, Y$_2$O$_3$, BaTiO$_3$, SrTiO$_3$, and BaZr$_{0.1}$Ce$_{0.7}$Y$_{0.1}$Yb$_{0.1}$O$_{3-\delta}$ (a proton conductor after hydration): At flash sintering temperatures, which must be well exceeding 1000 °C, they all have high O^{2-} conductivity and relatively low electronic conductivity and, thus, can be treated as solid electrolytes. In fact, the situations in flash sintering more often than not correspond to the extreme redox conditions described in Sections 2 and 3, for several reasons. First, a large voltage is used in most flash sintering experiments, which will at least push the electrodes outside the electrolytical window. Second, in a thermal runaway, the current density can reach very high values (up to ~100 A/cm^2, much higher than the values of ~1 A/cm^2 in a typical SOFC/SOEC at <1000 °C), so the electrode/sample interfaces must very rapidly convert the electronic current in the external circuit to the ionic current in the sample, which is likely to require a huge overpotential. As this overpotential is transferred into the interior of the electrolyte sample via the process described in Section 2, extreme redox conditions are set up, which can cause transverse and longitudinal damages. Not surprisingly, cracking and cavitation at grain boundaries have been observed,[73–76] and they manifest an orientation

preference, e.g., reduction voids formed at transverse grain boundaries.[74,75] Electrode conditions are obviously important. To lessen oxygen potential gradients and to produce samples with a more uniform microstructure, better electrodes with higher oxygen reduction/evolution reaction (ORR/OER) activities should be used. In fact, in cubic YSZ single crystals where there is no grain boundary damage but there is a measurable movement of the reduction front under a DC voltage, a large effect of electrode efficiency on the movement velocity is readily observable.[78]

Regarding the longitudinal mode of degradation in ceramic samples undergoing rapid heating and electrochemical reduction/oxidation, such a mode is typically associated with obvious instabilities such as the formation of hot spots and reduction filaments, which are exacerbated by larger voltages/current densities and poorer electrode/sample contacts. (More on instability in Section 5.) These instabilities can lead to localized sintering and abnormal microstructure as well as sample distortions and fractures. Examples are Figure 5.19 in ref 79 for YSZ, Figure 5 in ref 80 for GDC, Figures 37–40 in ref 81 for Al$_2$O$_3$, and Figure 5 in ref 82 for BaTiO$_3$.

Utilizing electromagnetic waves, laser-assisted surface treatment and welding of ceramics is another field-assisted processing technique.[83–85] It too produces microstructures similar to those observed in Figure 6a. Sharp grain size transitions are also identified (see examples of YSZ in Figure 6a in ref 83, inset of Figure 1a in ref 84, and Figure 3d in ref 85), which cannot be explained by the thermal effect alone, given the smoothly varying temperature profile, capped by melting, in the process zone. (However, rapid solidification after melting/welding could leave a directionally solidified microstructure.) In these techniques, since only a shallow surface layer is melted while the substrate is not, very likely there is a severe oxygen loss at the melt surface, but the loss next to the substrate should be negligible. If so, it would set up a steep reduction gradient similar to that of cathodic reduction in flash sintering, and such an extreme PO_2^{eq}/E_F gradient can cause a correspondingly extreme gradient in cation mobility,[86] thus producing a drastically graded microstructure.[83–85] Reduced, often-colored ceramics with hugely enhanced room-temperature electronic conductivity have been reported for YSZ as well as CeO$_2$, Bi$_2$O$_3$, TiO$_2$, Al$_2$O$_3$, NiO, ZnO, Fe$_2$O$_3$, V$_2$O$_3$, and NiO.[83] Similar effects could also be present in ceramics densified by other fast sintering and processing techniques.[87]
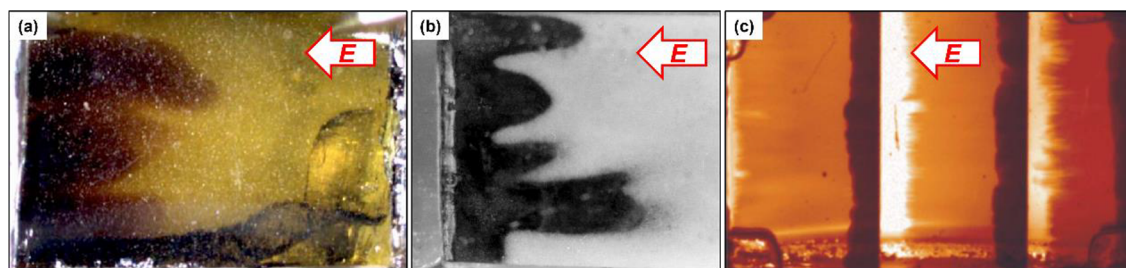
Figure 7. Electro-coloration of (a) $BaTiO_3$ single crystal (dark region reduced), (b) YSZ polycrystal (dark region reduced), and (c) Fe-doped $SrTiO_3$ tricrystal (dark region oxidized). (a) Reproduced with permission from ref 90. Copyright 2007 American Institute of Physics. (b) Reproduced with permission from ref 91. Copyright 1999 Published by Elsevier Science B.V. (c) Reproduced with permission from ref 94. Copyright 2017 Elsevier Ltd.

5. CERAMIC CAPACITORS AND MEMRISTORS

High permittivity ceramics such as titanates are widely used for capacitors. The most demanding application comes in the form of multilayer ceramic capacitors (MLCCs). In each MLCC, hundreds of thin oxide layers are packed and cofired with metal electrodes, which take a comb-like configuration to connect all the ceramic layers in parallel, resulting in a very high capacitance per unit volume. The same type of titanate ceramics is being developed for storing capacitive energy for fast discharge, and for certain power applications, they must withstand not only a high field but also a moderately high temperature. Another application is the gate oxide in a complementary metal–oxide semiconductor (CMOS), usually made of amorphous HfO_2, again an oxide of high permittivity. Titanates are semiconductors, but their oxygen vacancies, though slower, are still mobile at modest temperatures. Like zirconia and YSZ, HfO_2 is a wide bandgap insulator and oxygen-vacancy conductor. On the other hand, while the electric field in the above applications is higher or at least the same as in SOFC/SOEC and metal batteries, there is little electronic current (leakage) at their operating temperatures, i.e., these materials work as insulators. Interestingly, all the above insulators as well as many other ceramics have been developed into memristors, with a typical thickness of less than 100 nm, which are purposely made to "leak" electrons first by a high-voltage induced breakdown process called "forming". After this initiation process, two voltage-switchable resistance states can often develop, and both of them remain nonvolatile even after the (switching/reading) voltage is removed. The conducting paths in memristors are filamentary. Since the memristor material started as an insulator yet, once formed, the device does conduct electrons well at the ambient temperature, most likely the actual current density in the filament is much higher than the nominal current density. The present understanding of memristors is incomplete because of the nanoscale nature of conduction. But much is already known about the dielectric degradation of titanate capacitors. In addition, thanks to electro-coloration, direct visual observation of dielectric degradation can be made on the surfaces of polycrystals, and even three-dimensional observations have been made using transparent single crystals. Below we will utilize these direct studies and our general understanding of degradation in solid electrolytes to paint a plausible picture of degradation and other mechanisms in capacitors and memristors.

To begin with, we do not believe stress plays a very significant role here. This is because in capacitors and memristors chemical expansion/compression is likely to be small, internal bubble formation and metal deposition are minimal, and the thin film geometry will further limit the spatial range of stress

concentration. Regarding the oxygen potential distribution, which is important and will be discussed in detail later, we note here that it can obviously be affected by the distribution of electric field. Importantly, the electric field distribution in these devices made of highly insulating oxides is distinctly nonuniform to the extent that it also tends to be filamentary. We draw this conclusion from the following observations on zirconia and titanates.

Both zirconia (such as cubic and tetragonal YSZ) and titanates (such as $SrTiO_3$ and $BaTiO_3$, two prominent members of the perovskite family), when loaded under a constant voltage at a modest temperature between 200 and 300 °C, find their resistance gradually decreases and leakage gradually increases as if there is a uniform degradation in the sample. This is the test of DC electrical degradation,[88,89] which is routinely conducted to predict the service life. However, at an electric field comparable to that in actual device applications, the tested samples—both single crystals as in Figure 7a for $BaTiO_3$ and polycrystals as in Figure 7b for cubic YSZ—display a finger-like redox front that is visible because of electro-coloration of redox-sensitive color centers.[90,91] Similar finger-like redox fronts were also observed in both $SrTiO_3$[92] and YSZ[78] single crystals at comparable electric fields.

The above finger-like "interface" morphology is actually expected from the following stability analysis of the potential front in standard field equations and transport equations. First, in an insulator, a planar equipotential surface of the electric potential satisfying the Poisson equation is inherently unstable. This is seen in atmospheric lightning, which is an ionization/discharge process manifesting a filamentary electric driving field. Specifically, as the plane front of the equipotential is perturbed to become wavy, any protrusion on it will become a field concentrator, which leads to a higher local field that in turn leads to a higher local conductivity (which is the case both in lightening due to ionization and in an insulator due to dielectric breakdown), thus localizing the field further. This is the electrical basis of instability. Second, a planar conduction front satisfying the diffusion-transport equation is also inherently unstable. As the planar front is perturbed to become wavy, a protrusion having a smaller radius of curvature than the planar front sees a shorter diffusion distance (being of the order of the radius of curvature); thus, it will receive more influx, allowing the protrusion to grow faster and further. This is the diffusion/transport basis of instability. Inasmuch DC electrical degradation is no doubt driven by the electric field and involves charge transport, the inherent instabilities above dictate that the degradation paths tend to degenerate into filamentary ones, which are seen in Figure 7a,b as well as in ref 78 and ref 92. Not surprisingly, a stronger field/current/nonlinearity makes the
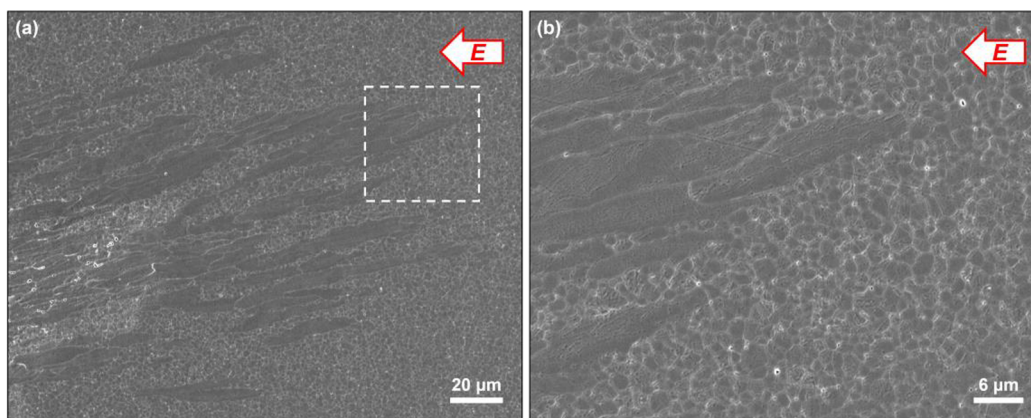
Figure 8. (a) Finger-/needle-like grain structure developed in DC-loaded tetragonal YSZ (3 mol % yttria-stabilized zirconia). (b) Enlarged view of the dashed box in (a). Loading conditions: DC current density 25 A/cm^2 for 20 h in air. Furnace temperature: 1200 °C. Sample thickness: 1.1 mm. Before high-temperature DC loading, the sample (prepared using TZ-3Y-E, Tosoh Co., Tokyo, Japan) was presintered at 1300 °C for 12 h to reach full density.

instability more difficult to suppress, and it will rapidly lead to filamentary growth across the two electrodes in thin-film devices such as MLCCs and memristors. This type of longitudinal mode of degradation is prominent in highly insulating ceramics and is commonly termed, loosely, dielectric breakdown. As mentioned already, a typical memristor must go through a forming step, which breaks down the highly insulating initial state into a much less resistive filamentary state, which makes the formed memristor switchable under a bipolar set of voltages. The forming process and the development of the conducting filament no doubt go through the above instability process.

We now turn to the distribution of PO_2^{eq}/E_F. First, consider the case of ionic-conductivity dominance, such as YSZ and HfO$_2$ in which the same oxygen potential transition discussed in Section 2 and depicted in Figure 1a should appear. However, in view of the low service temperature of capacitors and memristors, one might expect a long transient time before the steady-state potential is developed. But this may not be the case at all because of the much higher electric field and the much shorter sample thickness—the latter translates into a much shorter transient time since the diffusion time is proportional to the square of the diffusion distance. Second, consider the case of electronic-conduction dominance, such as SrTiO$_3$ and BaTiO$_3$ in which electronic conduction is primarily driven by the electric field and not by the redox potential. While one might conclude that this would render the oxygen potential transition irrelevant, this is not the case at all, as can be seen from the following consideration. In all the perovskites and many semiconducting oxides, oxygen vacancies are much more mobile than cations, and over time they migrate toward the cathode and accumulate there because, at the service temperatures of capacitors and memristors, cathodes being a metal are typically impenetrable to oxygen. This has been verified in SrTiO$_3$.[88,89,93] As a result of vacancy redistribution, an oxygen potential transition from the cathode to the anode is set up, and it eventually becomes steep enough to completely suppress the oxygen-vacancy flux. Such redox profiles that manifest in electro-coloration have been verified many times in the literature.[88,89,92,93] In addition to electrodes, grain boundaries can also block oxygen flow,[93] which is made evident in a model tricrystal experiment on SrTiO$_3$ (Figure 7c): It shows abruptly different redox potentials—manifested in sharply contrasting electro-coloration—on two sides of the two (transverse) grain boundaries.[94] The redox

potential transition vividly illustrated in Figure 7c is reminiscent of the oxygen potential jump/drop in Figure 3a,b, even though it is in a somewhat different transport regime from that in YSZ, for YSZ as well as any good electrolyte has a nearly constant oxygen-vacancy concentration throughout, which is not seen in titanates. Therefore, oxygen potential transitions and jumps at transverse boundaries are also possible in titanate (and most likely other) semiconductors even though they are not fast ion conductors, and their steady-state ionic disorder concentration can also vary by orders of magnitude.

We have reasons to believe such transverse grain boundaries can nucleate degradation. First, oxygen bubbles have been observed at the anode—electrode interface in SrTiO$_3$,[95] so the same possibility cannot be ruled out at oxygen-ion-blocking transverse grain boundaries. Moreover, it is known that the sharp redox transition between the cathode and the anode due to electrode blocking effectively turns the initially uniform semiconductor into a $p−n$ junction, with a p-region on the anode side and n-region on the cathode side, and only the junction between the two regions is highly resistive and mostly responsible for the residual resistance of the degraded sample. So the redox potential transition is at least directly responsible for DC electrical degradation. Lastly, as DC resistance degradation enters the final stage, we have observed oxygen egress from the anode in SrTiO$_3$ single crystals,[92] which is likely due to the coalescence of the above-mentioned oxygen bubbles, which makes an initially impenetrable electrode "leaky". We would expect the same to occur at transverse boundaries in a polycrystal, which would portend grain boundary degradation and even cracking. Thus, we believe there is a complete analogy of redox potential transition and damage development between semiconducting ceramics and fast ion electrolytes.

The above development of redox potential is relevant to memristors.[96,97] Although nonfilamentary electronic memristors not involving redox reactions are known,[98] it is generally agreed that filamentary memristors in which the initial filament is formed by cation movement must continue to rely on cation movement to reconnect the filament—filament disconnect in this case is due to Joule-heat-induced melting. (The other memristor type that forms the initial filament by anion movement may be subsequently switched largely electronically, by taking advantage of the polarity of the $p−n$ junction if the junction is very close to the forming anode.[99]) Such reconnect

action is very likely to occur in one short section (we will call it "gap" below) only, since the two halves of a disconnected filament may be regarded as virtual electrodes, electrically connected to one electrode each. While the gap distance is likely to be already short in a memristor, the "effective gap distance" could be even shorter if a robust redox potential transition can be established between them. This is because the effective thickness of the redox electrodes is actually close to the half-thickness of the electrolyte as shown in Figure 1a: On each side of the PO_2^{eq}/E_F transition, the redox potential is essentially the same as that of the electrode. Obviously, if a much shorter effective gap distance can be realized, it will make switching much faster. For this to happen, the field-transport-induced potential transition must closely follow the footstep of the instability, since the filament is itself a product of the field/transport instability. This is indeed the case as illustrated in Figure 8, taken from a tetragonal YSZ similarly DC electrically loaded as the cubic YSZ shown in Figure 6. Within the fully developed instability of very long fingers (more like needles, with aspect ratios up to ∼100), we find their grain sizes many times those of the grains outside; the latter had not grown at all since tetragonal YSZ, as mentioned before, has a very robust solute drag mechanism that can very effectively suppress grain growth under normal circumstances. Yet the hugely enhanced grain growth inside these fingers is irrefutable evidence that the solute drag is rendered completely ineffective by a hugely enhanced cation diffusivity in the lattice, which implies a hugely reducing condition as well as a hugely steep redox gradient.[73−75,86] Therefore, Figure 8 proves that the redox transition can closely follow the footstep of field/transport instability. Memristors in which cation movement dominates are made of oxides and chalcogenides that contain Cu^+, Ag^+, and Au^+. As a cation coming from the oxidized half next to the virtual anode migrates into the gap of a disconnected filament, we expect it to be promptly reduced to metallic once it enters the reduced half next to the virtual cathode. Therefore, cations only need to migrate a very short physical distance to reconnect a broken filament. This last case is especially interesting in that it illustrates how a redox transition of a *transverse* profile can facilitate the reconnection of filaments of a *longitudinal* profile.

6. CONCLUSIONS

The phenomenology and mechanisms of transverse and longitudinal degradations in ceramic solid electrolytes and insulators can be understood in terms of the characteristic distributions of redox potentials and oxygen partial pressures, stresses, and electric fields, none of which follows the often-assumed linear profiles interpolated from their boundary values. In many technology-relevant applications, the electric-field distribution is more a reflection of evolving instabilities than the steady state. In contrast, sharp step-function-like transitions of redox potentials become fully developed only at the steady state. Importantly, such transitions occur in both fast-ion conducting electrolytes and semiconducting insulators, but even more remarkably, they follow in lockstep the electric-field instabilities which can be quite complex. Unexpected stress distributions may originate from material insertion/removal or compositional changes compelled by the evolving transition of redox potentials, and via this connection they may additionally follow the electric-field instability as in the case of metallic dendrites. Despite such complexity, the stress distributions can often be predicted using a mean-field continuum analysis to quantitatively explain the damage phenomenology in ceramic solid electrolytes. Lessons learned from SOFC/SOEC/batteries are extended to multilayer

ceramic capacitors and memristors to anticipate and rationalize their damage phenomenology; in the case of memristors, they also explain the mechanisms of forming and filament reconnection. Furthermore, these lessons are relevant to field-assisted ceramic processing that relies on nonequilibrium, though somewhat controllable, techniques. General and specific strategies to mitigate damage and improve performance are proposed; the most intriguing among them and potentially reaping the most rewards is by purposeful doping that aims to precisely control global and local electronic conductivities. Other strategies, some already proven successful, include developing new solid electrolytes or composites with increased electrochemical and mechanical stabilities, designing better and more durable electrode–electrolyte interfaces with good contact and wetting that last for the entire service life, and lowering electrode overpotentials by developing and better integrating highly active efficient electrodes and/or electrode catalysts. The above understanding and mitigation strategies are expected to be most useful when the technology extends to more extreme and demanding operation conditions, which are rapidly materializing in rechargeable metal batteries[100] and emerging electrochemical devices.

■ AUTHOR INFORMATION

Corresponding Authors

Yanhao Dong — *Department of Nuclear Science and Engineering, Massachusetts Institute of Technology, Cambridge, Massachusetts 02139, United States;* ⊙ orcid.org/0000-0003-1224-1015; Email: dongyh@mit.edu

I-Wei Chen — *Department of Materials Science and Engineering, University of Pennsylvania, Philadelphia, Pennsylvania 19104, United States;* Email: iweichen@seas.upenn.edu

Ju Li — *Department of Nuclear Science and Engineering and Department of Materials Science and Engineering, Massachusetts Institute of Technology, Cambridge, Massachusetts 02139, United States;* ⊙ orcid.org/0000-0002-7841-8058; Email: liju@mit.edu

Complete contact information is available at:
https://pubs.acs.org/10.1021/acs.chemmater.2c00329

Notes

The authors declare no competing financial interest.

Biographies

Yanhao Dong is a postdoctoral researcher at Massachusetts Institute of Technology (MIT). He obtained his B.S. degree in materials science in 2012 from Tsinghua University and his Ph.D. degree in materials science in 2017 from the University of Pennsylvania (Penn). His current research interest is in the design, synthesis, and processing of ceramics and other materials, especially those for energy applications.

I-Wei Chen is the Skirkanich Professor of Materials Innovation at Penn, with former appointments at the University of Michigan and MIT. He obtained his B.S. degree in physics in 1972 from National Tsinghua University, Taiwan, his M.S. degree in physics in 1975 from Penn, and his Ph.D. degree in metallurgy in 1980 from MIT. His current research interest is in thin-film memory devices, energy ceramics, and drug delivery.

Ju Li is the Battelle Energy Alliance Professor in Nuclear Engineering and Professor of Materials Science and Engineering at MIT. His group performs computational and experimental research on mechanical

properties of materials and energy storage and conversion. He obtained his Ph.D. degree in nuclear engineering in 2000 from MIT.

ACKNOWLEDGMENTS

REFERENCES

(1) Goodenough, J. B. Ceramic Solid Electrolytes. *Solid State Ionics* **1997**, *94*, 17−25.

(2) Graves, C.; Ebbesen, S. D.; Jensen, S. H.; Simonsen, S. B.; Mogensen, M. B. Eliminating Degradation in Solid Oxide Electrochemical Cells by Reversible Operation. *Nat. Mater.* **2015**, *14*, 239−244.

(3) Choi, S.; Kucharczyk, C. J.; Liang, Y.; Zhang, X.; Takeuchi, I.; Ji, H.-I.; Haile, S. M. Exceptional Power Density and Stability at Intermediate Temperatures in Protonic Ceramic Fuel Cells. *Nat. Energy* **2018**, *3*, 202−210.

(4) Han, X.; Gong, Y.; Fu, K.; He, X.; Hitz, G. T.; Dai, J.; Pearse, A.; Liu, B.; Wang, H.; Rubloff, G.; Mo, Y.; Thangadurai, V.; Wachsman, E. D.; Hu, L. Negating Interfacial Impedance in Garnet-based Solid-State Li Metal Batteries. *Nat. Mater.* **2017**, *16*, 572−579.

(5) Tan, A. J.; Huang, M.; Avci, C. O.; Buttner, F.; Mann, M.; Hu, W.; Mazzoli, C.; Wilkins, S.; Tuller, H. L.; Beach, G. S. D. Magneto-Ionic Control of Magnetism Using a Solid-State Proton Pump. *Nat. Mater.* **2019**, *18*, 35−41.

(6) De Jonghe, L. C.; Feldman, L.; Beuchele, A. Slow Degradation and Electron Conduction in Sodium/Beta-Aluminas. *J. Mater. Sci.* **1981**, *16*, 780−786.

(7) De Jonghe, L. C.; Feldman, L.; Buechele, A. Failure Modes of Na-Beta Alumina. *Solid State Ionics* **1981**, *5*, 267−269.

(8) Ren, Y.; Shen, Y.; Lin, Y.; Nan, C.-W. Direct Observation of Lithium Dendrites inside Garnet-Type Lithium-Ion Solid Electrolyte. *Electrochem. Commun.* **2015**, *57*, 27−30.

(9) Aguesse, F.; Manalastas, W.; Buannic, L.; Lopez del Amo, J. M.; Singh, G.; Llordes, A.; Kilner, J. Investigating the Dendritic Growth during Full Cell Cycling of Garnet Electrolyte in Direct Contact with Li Metal. *ACS Appl. Mater. Interfaces* **2017**, *9*, 3808−3816.

(10) Laguna-Bercero, M. A.; Campana, R.; Larrea, A.; Kilner, J. A.; Orera, V. M. Electrolyte Degradation in Anode Supported Microtubular Yttria Stabilized Zirconia-based Solid Oxide Steam Electrolysis Cells at High Voltages of Operation. *J. Power Sources* **2011**, *196*, 8942−8947.

(11) Tietz, F.; Sebold, D.; Brisse, A.; Schefold, J. Degradation Phenomena in a Solid Oxide Electrolysis Cell after 9000 h of Operation. *J. Power Sources* **2013**, *223*, 129−135.

(12) Mocoteguy, P.; Brisse, A. A Review and Comprehensive Analysis of Degradation Mechanisms of Solid Oxide Electrolysis Cells. *Int. J. Hydrog. Energy* **2013**, *38*, 15887−15902.

(13) Wang, Y.; Li, W.; Ma, L.; Li, W.; Liu, X. Degradation of Solid Oxide Electrolysis Cells: Phenomena, Mechanisms, and Emerging Mitigation Strategies—A Review. *J. Mater. Sci. Technol.* **2020**, *55*, 35−55.

(14) Morales, M.; Roa, J. J.; Tartaj, J.; Segarra, M. A Review of Doped Lanthanum Gallates as Electrolytes for Intermediate Temperature Solid Oxide Fuel Cells: From Materials Processing to Electrical and Thermomechanical Properties. *J. Eur. Ceram. Soc.* **2016**, *36*, 1−16.

(15) Kim, K.-J.; Choi, S.-W.; Kim, M.-Y.; Lee, M.-S.; Kim, Y.-S.; Kim, H.-S. Fabrication Characteristics of SOFC Single Cell with Thin LSGM Electrolyte via Tape-Casting and Co-Sintering. *J. Ind. Eng. Chem.* **2016**, *42*, 69−74.

(16) Ishihara, T.; Wang, S.; Wu, K.-T. Highly Active Oxide Cathode of La(Sr)Fe(Mn)O$_3$ for Intermediate Temperature CO$_2$ and CO$_2$-H$_2$O Co-Electrolysis Using LSGM Electrolyte. *Solid State Ionics* **2017**, *299*, 60−63.

(17) Kim, J.-H.; Yoo, H.-I. Partial Electronic Conductivity and Electrolytic Domain of La$_{0.9}$Sr$_{0.1}$Ga$_{0.8}$Mg$_{0.2}$O$_{3−\delta}$. *Solid State Ionics* **2001**, *140*, 105−113.

(18) Virkar, A. V. Mechanism of Oxygen Electrode Delamination in Solid Oxide Electrolyzer Cells. *Int. J. Hydrog. Energy* **2010**, *35*, 9527−9543.

(19) Jacobsen, T.; Mogensen, M. The Course of Oxygen Partial Pressure and Electric Potentials across an Oxide Electrolyte Cell. *ECS Trans.* **2008**, *13*, 259−273.

(20) Dong, Y.; Chen, I.-W. Oxygen Potential Transition in Mixed Conducting Oxide Electrolyte. *Acta Mater.* **2018**, *156*, 399−410.

(21) Park, J.-H.; Blumenthal, R. N. Electric Transport in 8 Mole Percent Y$_2$O$_3$-ZrO$_2$. *J. Electrochem. Soc.* **1989**, *136*, 2867−2876.

(22) Dong, Y.; Huang, Y.; Ding, D.; Wu, W.; Yao, X.; Li, J. Chemical and Structural Origin of Hole States in Yttria-Stabilized Zirconia. *Acta Mater.* **2021**, *203*, 116487.

(23) Knibbe, R.; Traulsen, M. L.; Hauch, A.; Ebbesen, S. D.; Mogensen, M. Solid Oxide Electrolysis Cells: Degradation at High Current Densities. *J. Electrochem. Soc.* **2010**, *157*, B1209−B1217.

(24) Nechache, A.; Boukamp, B. A.; Cassir, M.; Ringuede, A. Accelerated Degradation of Yttria Stabilized Zirconia Electrolyte during High-Temperature Water Electrolysis. *J. Solid State Electrochem.* **2019**, *23*, 871−881.

(25) Dong, Y.; Zhang, Z.; Alvarez, A.; Chen, I.-W. Potential Jumps at Transport Bottlenecks Cause Instability of Nominally Ionic Solid Electrolytes in Electrochemical Cells. *Acta Mater.* **2020**, *199*, 264−277.

(26) Marrocchelli, D.; Bishop, S. R.; Tuller, H. L.; Yildiz, B. Understanding Chemical Expansion in Non-Stoichiometric Oxides: Ceria and Zirconia Case Studies. *Adv. Funct. Mater.* **2012**, *22*, 1958−1965.

(27) Ruh, R.; Garrett, H. J. Nonstoichiometry of ZrO$_2$ and its Relation to Tetragonal-Cubic Inversion in ZrO$_2$. *J. Am. Ceram. Soc.* **1967**, *50*, 257−261.

(28) Lenser, C.; Zhang, J.; Russner, N.; Weber, A.; Guillon, O.; Menzler, N. Electro-Chemo-Mechanical Failure in a High-Performance Solid Oxide Cell. *Meet. Abstr.* **2021**, *MA2021-03*, 78.

(29) Choi, S.; Kucharczyk, C. J.; Liang, Y.; Zhang, X.; Takeuchi, I.; Ji, H.-I.; Haile, S. M. Exceptional Power Density and Stability at Intermediate Temperatures in Protonic Ceramic Fuel Cells. *Nat. Energy* **2018**, *3*, 202−210.

(30) Pergolesi, D.; Fabbri, E.; D'Epifanio, A.; Di Bartolomeo, E.; Tebano, A.; Sanna, S.; Licoccia, S.; Balestrino, G.; Traversa, E. High Proton Conduction in Grain-Boundary-Free Yttrium-Doped Barium Zirconate Films Grown by Pulsed Laser Deposition. *Nat. Mater.* **2010**, *9*, 846−852.

(31) Menon, M.; Chen, I.-W. Bimaterial Composites via Colloidal Rolling Techniques: II, Sintering Behavior and Thermal Stresses. *J. Am. Ceram. Soc.* **1999**, *82*, 3422−3429.

(32) Giuntini, D.; Chen, I.-W.; Olevsky, E. A. Sintering Shape Distortions Controlled by Interface Roughness in Powder Composites. *Scripta Mater.* **2016**, *124*, 38−41.

(33) Bian, W.; Wu, W.; Wang, B.; Tang, W.; Zhou, M.; Jin, C.; Ding, H.; Fan, W.; Dong, Y.; Li, J.; Ding, D. Revitalizing Interface in Protonic Ceramic Cells by Acid Etch. *Nature* **2022**, *604*, 479−485.

(34) Cao, T.; Cheng, Y.; Gorte, R. J.; Shi, Y.; Vohs, J. M.; Cai, N. Effect of Grain Boundary Diffusion on Electrolyte Stability in Direct Carbon Fuel Cells with Antimony Anodes. *Ceram. Int.* **2017**, *43*, 16575−16579.

(35) Mogensen, M. B. Materials for Reversible Solid Oxide Cells. *Curr. Opin. Electrochem.* **2020**, *21*, 265−273.

(36) Wachsman, E. D.; Lee, K. T. Lowering the Temperature of Solid Oxide Fuel Cells. *Science* **2011**, *334*, 935−939.

(37) Chatzichristodoulou, C.; Chen, M.; Hendriksen, P. V.; Jacobsen, T.; Mogensen, M. B. Understanding Degradation of Solid Oxide Electrolysis Cells through Modeling of Electrochemical Potential Profiles. *Electrochem. Acta* **2016**, *189*, 265−282.

(38) Park, B.-K.; Zhang, Q.; Voorhees, P. W.; Barnett, S. A. Conditions for Stable Operation of Solid Oxide Electrolysis Cells: Oxygen Electrode Effects. *Energy Environ. Sci.* **2019**, *12*, 3053−3062.

(39) Ning, Z.; Jolly, D. S.; Li, G.; De Meyere, R.; Pu, S. D.; Chen, Y.; Kasemchainan, J.; Ihli, J.; Gong, C.; Liu, B.; Melvin, D. L. R.; Bonnin, A.; Magdysyuk, O.; Adamson, P.; Hartley, G. O.; Monroe, C. W.; Marrow, T. J.; Bruce, P. G. Visualizing Plating-Induced Cracking in

Lithium-Anode Solid-Electrolyte Cells. *Nat. Mater.* **2021**, *20*, 1121−1129.

(40) Zhao, J.; Tang, Y.; Dai, Q.; Du, C.; Zhang, Y.; Xue, D.; Chen, T.; Chen, J.; Wang, B.; Yao, J.; Zhao, N.; Li, Y.; Xia, S.; Guo, X.; Harris, S. J.; Zhang, L.; Zhang, S.; Zhu, T.; Huang, J. In situ Observation of Li Deposition-Induced Cracking in Garnet Solid Electrolytes. *Energy Environ. Mater.* **2022**, *5*, 524−532.

(41) Porz, L.; Swamy, T.; Sheldon, B. W.; Rettenwander, D.; Fromling, T.; Thaman, H. L.; Berendts, S.; Uecker, R.; Carter, W. C.; Chiang, Y.-M. Mechanism of Lithium Metal Penetration through Inorganic Solid Electrolytes. *Adv. Energy Mater.* **2017**, *7*, 1701003.

(42) Swamy, T.; Park, R.; Sheldon, B. W.; Rettenwander, D.; Porz, L.; Berendts, S.; Uecker, R.; Carter, W. C.; Chiang, Y.-M. Lithium Metal Penetration Induced by Electrodeposition through Solid Electrolytes: Example in Single-Crystal $Li_6La_3ZrTaO_{12}$ Garnet. *J. Electrochem. Soc.* **2018**, *165*, A3648−A3655.

(43) Kazyak, E.; Garcia-Mendez, R.; LePage, W. S.; Sharafi, A.; Davis, A. L.; Sanchez, A. J.; Chen, K.-H.; Haslam, C.; Sakamoto, J.; Dasgupta, N. P. Li Penetration in Ceramic Solid Electrolytes: Operando Microscopy Analysis of Morphology, Propagation, and Reversibility. *Matter* **2020**, *2*, 1025−1048.

(44) Li, Y.; Chen, X.; Dolocan, A.; Cui, Z.; Xin, S.; Xue, L.; Xu, H.; Park, K.; Goodenough, J. B. Garnet Electrolyte with an Ultralow Interfacial Resistance for Li-Metal Batteries. *J. Am. Chem. Soc.* **2018**, *140*, 6448−6455.

(45) Chen, Y.; Wang, Z.; Li, X.; Yao, X.; Wang, C.; Li, Y.; Xue, W.; Yu, D.; Kim, S. Y.; Yang, F.; Kushima, A.; Zhang, G.; Huang, H.; Wu, N.; Mai, Y.-W.; Goodenough, J. B.; Li, J. Li Metal Deposition and Stripping in a Solid-State Battery via Coble Creep. *Nature* **2020**, *578*, 251−255.

(46) Huo, H.; Chen, Y.; Li, R.; Zhao, N.; Luo, J.; Pereira da Silva, J. G.; Mucke, R.; Kaghazchi, P.; Guo, X.; Sun, X. Design of a Mixed Conductive Garnet/Li Interface for Dendrite-Free Solid Lithium Metal Batteries. *Energy Environ. Sci.* **2020**, *13*, 127−134.

(47) Liu, X.; Garcia-Mendez, R.; Lupini, A. R.; Cheng, Y.; Hood, Z. D.; Han, F.; Sharafi, A.; Idrobo, J. C.; Dudney, N. J.; Wang, C.; Ma, C.; Sakamoto, J.; Chi, M. Local Electronic Structure Variation Resulting in Li 'Filament' Formation within Solid Electrolytes. *Nat. Mater.* **2021**, *20*, 1485−1490.

(48) Cheng, E. J.; Sharafi, A.; Sakamoto, J. Intergranular Li Metal Propagation through Polycrystalline $Li_{6.25}Al_{0.25}La_3Zr_2O_{12}$ Ceramic Electrolyte. *Electrochem. Acta* **2017**, *223*, 85−91.

(49) Chen, L.; Huang, Z.; Pang, W.; Jin, Z.; Li, Y.; Wang, C.-A. Dual Interface Layers for Solid-State Li Metal Battery with Low Interfacial Resistance and Small Polarization based on Garnet Electrolyte. *Electrochem. Acta* **2020**, *330*, 135352.

(50) Song, Y.; Yang, L.; Zhao, W.; Wang, Z.; Zhao, Y.; Wang, Z.; Zhao, Q.; Liu, H.; Pan, F. Revealing the Short-Circuiting Mechanism of Garnet-based Solid-State Electrolyte. *Adv. Energy Mater.* **2019**, *9*, 1900671.

(51) Balaish, M.; Gonzalez-Rosillo, J. C.; Kim, K. J.; Zhu, Y.; Hood, Z. D.; Rupp, J. L. M. Processing Thin but Robust Electrolytes for Solid-State Batteries. *Nat. Energy* **2021**, *6*, 227−239.

(52) Dong, Y.; Yang, H.; Zhang, L.; Li, X.; Ding, D.; Wang, X.; Li, J.; Li, J.; Chen, I.-W. Ultra-Uniform Nanocrystalline Materials via Two-Step Sintering. *Adv. Funct. Mater.* **2021**, *31*, 2007750.

(53) Krauskopf, T.; Richter, F. H.; Zeier, W. G.; Janek, J. Physicochemical Concepts of the Lithium Metal Anode in Solid-State Batteries. *Chem. Rev.* **2020**, *120*, 7745−7794.

(54) Han, F.; Westover, A. S.; Yue, J.; Fan, X.; Wang, F.; Chi, M.; Leonard, D. N.; Dudney, N. J.; Wang, H.; Wang, C. High Electronic Conductivity as the Origin of Lithium Dendrite Formation within Solid Electrolytes. *Nat. Energy* **2019**, *4*, 187−196.

(55) Wang, Y.; Virkar, A. V.; Zhou, X.-D. On the Thermodynamic Origin of the Formation of Li-Dendrites in an Electrochemical Cell. *J. Electrochem. Soc.* **2021**, *168*, 100503.

(56) Hassold, G. N.; Chen, I.-W.; Srolovitz, D. J. Computer Simulation of Final-Stage Sintering: I, Model Kinetics, and Microstructure. *J. Am. Ceram. Soc.* **1990**, *73*, 2857−2864.

(57) Chen, I.-W. Model of Transformation Toughening in Brittle Materials. *J. Am. Ceram. Soc.* **1991**, *74*, 2564−2572.

(58) Wen, Z.; Gu, Z.; Xu, X.; Cao, J.; Zhang, F.; Lin, Z. Research Activities in Shanghai Institute of Ceramics, Chinese Academy of Sciences on the Solid Electrolytes for Sodium Sulfur Batteries. *J. Power Sources* **2008**, *184*, 641−645.

(59) Reyes-Morel, P. E.; Chen, I.-W. Transformation Plasticity of Ce-TZP I. Stress Assistance and Autocatalysis. *J. Am. Ceram. Soc.* **1988**, *71*, 343−353.

(60) Xue, L. A.; Meyer, K.; Chen, I.-W. Control of Grain Boundary Pinning in Al_2O_3/ZrO_2 Composites with Ce^{3+}/Ce^{4+} Doping. *J. Am. Ceram. Soc.* **1992**, *75*, 822−829.

(61) Deng, T.; Ji, X.; Zou, L.; Chiekezi, O.; Cao, L.; Fan, X.; Adebisi, T. R.; Chang, H.-J.; Wang, H.; Li, B.; Li, X.; Wang, C.; Reed, D.; Zhang, J.-G.; Sprenkle, V. L.; Wang, C.; Lu, X. Interfacial-Engineering-Enabled Practical Low-Temperature Sodium Metal Battery. *Nat. Nanotechnol.* **2022**, *17*, 269−277.

(62) Hwang, S. L.; Chen, I.-W. Grain Size Control of Tetragonal Zirconia Polycrystals Using the Space Charge Concept. *J. Am. Ceram. Soc.* **1990**, *73*, 3269−3277.

(63) Pfenninger, R.; Struzik, M.; Garbayo, I.; Stilp, E.; Rupp, J. L. M. A Low Ride on Processing Temperature for Fast Lithium Conduction in Garnet Solid-State Battery Films. *Nat. Energy* **2019**, *4*, 475−483.

(64) Hitz, G. T.; McOwen, D. W.; Zhang, L.; Ma, Z.; Fu, Z.; Wen, Y.; Gong, H.; Dai, J.; Hamann, T. R.; Hu, L.; Wachsman, E. D. High-Rate Lithium Cycling in a Scalable Trilayer Li-Garnet-Electrolyte Architecture. *Mater. Today* **2019**, *22*, 50−57.

(65) Thomas-Alyea, K. E. Design of Porous Solid Electrolytes for Rechargeable Metal Batteries. *J. Electrochem. Soc.* **2018**, *165*, A1523−A1528.

(66) Bates, J. B.; Dudney, N. J.; Gruzalski, G. R.; Zuhr, R. A.; Choudhury, A.; Luck, C. F.; Robertson, J. D. Electrical Properties of Amorphous Lithium Electrolyte Thin Films. *Solid State Ionics* **1992**, *53-56*, 647−654.

(67) An, J.; Kim, Y.-B.; Park, J.; Gur, T. M.; Prinz, F. B. Three-Dimensional Nanostructured Bilayer Solid Oxide Fuel Cell with 1.3 W/ cm^2 at 450 °C. *Nano Lett.* **2013**, *13*, 4551−4555.

(68) Cologna, M.; Rashkova, B.; Raj, R. Flash Sintering of Nanograin Zirconia in < 5 s at 850 °C. *J. Am. Ceram. Soc.* **2010**, *93*, 3556−3559.

(69) Downs, J. A.; Sglavo, V. M. Electric Field Assisted Sintering of Cubic Zirconia at 390 °C. *J. Am. Ceram. Soc.* **2013**, *96*, 1342−1344.

(70) Dong, Y.; Chen, I.-W. Onset Criterion for Flash Sintering. *J. Am. Ceram. Soc.* **2015**, *98*, 3624−3627.

(71) Todd, R. I.; Zapata-Solvas, E.; Bonilla, R. S.; Sneddon, T.; Wilshaw, P. R. Electrical Characteristics of Flash Sintering: Thermal Runaway of Joule Heating. *J. Eur. Ceram. Soc.* **2015**, *35*, 1865−1877.

(72) Zhang, Y.; Jung, J.-I.; Luo, J. Thermal Runaway, Flash Sintering and Asymmetrical Microstructural Development of ZnO and ZnO-Bi_2O_3 under Direct Currents. *Acta Mater.* **2015**, *94*, 87−100.

(73) Kim, S.-W.; Kim, S. G.; Jung, J.-I.; Kang, S.-J. L.; Chen, I.-W. Enhanced Grain Boundary Mobility in Yttria-Stabilized Cubic Zirconia under an Electric Current. *J. Am. Ceram. Soc.* **2011**, *94*, 4231−4238.

(74) Dong, Y.; Wang, H.; Chen, I.-W. Electrical and Hydrogen Reduction Enhances Kinetics in Doped Zirconia and Ceria: I. Grain Growth Study. *J. Am. Ceram. Soc.* **2017**, *100*, 876−886.

(75) Dong, Y.; Chen, I.-W. Electrical and Hydrogen Reduction Enhances Kinetics in Doped Zirconia and Ceria: II. Mapping Electrode Polarization and Vacancy Condensation in YSZ. *J. Am. Ceram. Soc.* **2018**, *101*, 1058−1073.

(76) Nie, J.; Hu, C.; Yan, Q.; Luo, J. Discovery of Electrochemically Induced Grain Boundary Transitions. *Nat. Commun.* **2021**, *12*, 2374.

(77) Charalambous, H.; Jha, S. K.; Wang, H.; Phuah, X. L.; Wang, H.; Tsakalakos, T. Inhomogeneous Reduction and its Relation to Grain Growth of Titania during Flash Sintering. *Scripta Mater.* **2018**, *155*, 37−40.

(78) Alvarez, A.; Dong, Y.; Chen, I.-W. DC Electrical Degradation of YSZ: Voltage-Controlled Electrical Metallization of a Fast Ion Conducting Insulator. *J. Am. Ceram. Soc.* **2020**, *103*, 3178−3193.

(79) Downs, J. A. Mechanisms of Flash Sintering in Cubic Zirconia. Ph.D. Thesis, University of Trento, Trento, Italy, 2013.

(80) Mishra, T. P.; Lenser, C.; Raj, R.; Guillon, O.; Bram, M. Development of a Processing Map for Safe Flash Sintering of Gadolinium-Doped Ceria. *J. Am. Ceram. Soc.* **2021**, *104*, 4316−4328.

(81) Biesuz, M. Flash Sintering of Alumina-based Ceramics. Ph.D. Thesis, University of Trento, Trento, Italy, 2017.

(82) Shi, R.; Pu, Y.; Ji, J.; Li, J.; Guo, X.; Wang, W.; Yang, M. Correlation between Flash Sintering and Dielectric Breakdown Behavior in Donor-Doped Barium Titanate Ceramics. *Ceram. Int.* **2020**, *46*, 12846−12851.

(83) Song, L.; Ma, J.; Zhang, Q.; Shen, Z. Laser Melted Oxide Ceramics: Multiscale Structural Evolution with Non-Equilibrium Features. *J. Materionics* **2019**, *5*, 436−445.

(84) Song, L.; Zhang, Q.; Ma, J.; Chen, C.; Xu, B.; Zhu, M.; Xu, X.; Nan, C.; Shen, Z. Vacancy-Ordered Yttria Stabilized Zirconia as a Low-Temperature Electronic Conductor Achieved by Laser Melting. *J. Eur. Ceram. Soc.* **2019**, *39*, 1374−1380.

(85) Penilla, E. H.; Devia-Cruz, L. F.; Wieg, A. T.; Martinez-Torres, P.; Cuando-Espitia, N.; Sellappan, P.; Kodera, Y.; Aguilar, G.; Garay, J. E. Ultrafast Laser Welding of Ceramics. *Science* **2019**, *365*, 803−808.

(86) Dong, Y.; Qi, L.; Alvarez, A.; Li, J.; Chen, I.-W. Enhanced Mobility of Cations and Anions in the Redox State: The Polaronium Mechanism. *Acta Mater.* **2022**, *232*, 117941.

(87) Wang, C.; Ping, W.; Bai, Q.; Cui, H.; Hensleigh, R.; Wang, R.; Brozena, A. H.; Xu, Z.; Dai, J.; Pei, Y.; Zheng, C.; Pastel, G.; Gao, J.; Wang, X.; Wang, H.; Zhao, J.-C.; Yang, B.; Zheng, X.; Luo, J.; Mo, Y.; Dunn, B.; Hu, L. A General Method to Synthesize and Sinter Bulk Ceramics in Seconds. *Science* **2020**, *368*, 521−526.

(88) Waser, R.; Baiatu, T.; Hardtl, K.-H. DC Electrical Degradation of Perovskite-Type Titanates: I, Ceramics. *J. Am. Ceram. Soc.* **1990**, *73*, 1645−1653.

(89) Waser, R.; Baiatu, T.; Hardtl, K.-H. DC Electrical Degradation of Perovskite-Type Titanates: II, Single Crystals. *J. Am. Ceram. Soc.* **1990**, *73*, 1654−1662.

(90) Yoo, H.-I.; Chang, M.-W.; Oh, T.-S.; Lee, C.-E.; Becker, K. D. Electrocoloration and Oxygen Vacancy Mobility of $BaTiO_3$. *J. Appl. Phys.* **2007**, *102*, 093701.

(91) Janek, J.; Korte, C. Electrochemical Blackening of Yttria-Stabilized Zirconia − Morphological Instability of the Moving Reaction Front. *Solid State Ionics* **1999**, *116*, 181−195.

(92) Alvarez, A.; Chen, I.-W. DC Resistance Degradation of $SrTiO_3$: The Role of Virtual-Cathode Needles and Oxygen Bubbles. *J. Am. Ceram. Soc.* **2022**, *105*, 362−383.

(93) Baiatu, T.; Waser, R.; Hardtl, K.-H. DC Electrical Degradation of Perovskite-Type Titanates: III, A Model of the Mechanism. *J. Am. Ceram. Soc.* **1990**, *73*, 1663−1673.

(94) Gregori, G.; Merkle, R.; Maier, J. Ion Conduction and Redistribution at Grain Boundaries in Oxide Systems. *Prog. Mater. Sci.* **2017**, *89*, 252−305.

(95) Wojtyniak, M.; Szot, K.; Wrzalik, R.; Rodenbucher, C.; Roth, G.; Waser, R. Electro-Degradation and Resistive Switching of Fe-Doped $SrTiO_3$ Single Crystal. *J. Appl. Phys.* **2013**, *113*, 083713.

(96) Wang, Z.; Wu, H.; Burr, G. W.; Hwang, C. S.; Wang, K. L.; Xia, Q.; Yang, J. J. Resistive Switching Materials for Information Processing. *Nat. Rev. Mater.* **2020**, *5*, 173−195.

(97) Yao, X.; Klyukin, K.; Lu, W.; Onen, M.; Ryu, S.; Kim, D.; Emond, N.; Waluyo, I.; Hunt, A.; del Alamo, J. A.; Li, J.; Yildiz, B. Protonic Solid-State Electrochemical Synapse for Physical Neural Networks. *Nat. Commun.* **2020**, *11*, 3134.

(98) Lu, Y.; Alvarez, A.; Kao, C.-H.; Bow, J.-S.; Chen, S.-Y.; Chen, I.-W. An Electronic Silicon-based Memristor with a High Switching Uniformity. *Nat. Electron.* **2019**, *2*, 66−74.

(99) Muenstermann, R.; Menke, T.; Dittmann, R.; Waser, R. Coexistence of Filamentary and Homogeneous Resistive Switching in Fe-Doped $SrTiO_3$ Thin-Film Memristive Devices. *Adv. Mater.* **2010**, *22*, 4819−4822.

(100) Goodenough, J. B.; Kim, Y. Challenges for Rechargable Li Batteries. *Chem. Mater.* **2010**, *22*, 587−603.